

**Appendices for the Paper: Design and Analysis of a High-Accuracy Version
of the Relativity-Gyro Experiment. Deposited in the PHYSICS
AUXILIARY PUBLICATION SERVICE for PRD15.**

Benjamin Lange
1922 Page Street, San Francisco, CA, 94117-1804
Fax: (415) 221-5335, email: blange@sanfrancisco.net

Appendix A. Calculations of the Major Gyro Drifts	1
Appendix A1. The Physical Basis of the Gravity-Gradient Drift	2
Appendix A2. The Gravity-Gradient-Drift Errors	2
Appendix A3. Magnetic-Eddy-Current, Barnett-Effect, and Spinning-Charge Drifts	5
Appendix A4. Roll Averaging	6
Appendix A5. Gas Brownian Motion and Gas Spin-Down Drifts	7
Appendix A6. Rotor Collisions with Large Particles in the Cavity	8
Appendix A7. Flat Differential Pressure	8
Appendix A8. Electric Fields in the Cavity	8
Appendix B. Zero-Gravity-Gradient Orbits.....	9
Appendix C. Autocollimator Performance.....	10
Appendix C1. Autocollimator Noise Equivalent Angle.....	11
Appendix C2. Autocollimator Zero-Point Errors	12
Appendix C3. Autocollimator Scale-Factor Errors	13
Appendix C4. Transcollimator.....	14
Appendix D. Summary of the Technique for Placing the Optical Flats on the Rotor.....	14
Appendix E. Telescope Performance	16
Appendix E1 Telescope Noise Equivalent Angle	16
Appendix E2. Telescope Zero-Point Errors.....	17
Appendix E3. Telescope Scale-Factor Errors.....	18
Appendix F. Roll-Coupled Zero-Point Errors and Drifts.....	22
Appendix G. Instrument Scale-Factor Calibration Accuracy	25
Appendix H. Operational and Miscellaneous Considerations.....	27
Appendix H1. Entering the Counter-Rotating Orbits.....	27
Appendix H2. Radiation Environment	27
Appendix H3. Active Damping	28
Appendix H4. Absolute Temperature Control	28
Appendix H5. Planetary Structure of the Reference Star.....	28
Appendix H6. Testing	28
Appendix H7. Four Gyros Versus One	28
References.....	29
Detailed Acknowledgments.....	30

Appendix A. Calculations of the Major Gyro Drifts

This appendix will emphasize the largest sources of gyro drift as well as those which were not tested by the 1972 drag-free flight [39]. These include gravity gradient, magnetic, gas brownian motion, large-particle, and spurious electric-field drifts. The balance of the drifts can be calculated from the expressions in Table 2 or can be found in References 2 or 32. The coordinate system used in the appendices is the gyro-

frame with the z -axis parallel to the gyro angular momentum axis and the x -axis as close to the earth's spin axis at J2000.0 as possible. With this definition, the axis which measures the geodetic drift is rotation about the y -axis (the experiment axis); and rotation about the x -axis is the cross axis, i.e. the axis used to measure the gyro performance and/or the frame-dragging drift.

Appendix A1. The Physical Basis of the Gravity-Gradient Drift

The first question which should arise in a design with an autocollimator readout is will the optical flats cause unacceptable gyro drift by making the surface nonspherical and by unbalancing the principal moments of inertia? It can be seen from the table of gyro drifts that the effect of the flats on drifts from torques due to surface forces is negligible. The gravity-gradient drift, however, is directly proportional to the moment-of-inertia difference ratio, $\Delta I/I = \varepsilon_T$, i.e. $\varepsilon_{Total} \cdot \varepsilon_T$ arises from two sources, a permanent $\Delta I/I = \varepsilon_p$ and an elastic $\Delta I/I = \varepsilon_{elastic}$ caused by the rotor spin. ε_p comes from the slightly nonspherical surface, density inhomogeneities, and the optical flats which are its primary cause. When two optical flats are ground onto the north and south poles of the rotor, the resulting permanent $\Delta I/I$ is given by $\varepsilon_p = 15(d_f/d_r)^4/16$ where d_f is the diameter of the flat and d_r is the rotor diameter. Thus two optical flats 5 mm in diameter on a 5-cm diameter rotor give $\varepsilon_p \approx 10^{-4}$. This is about 100 times as large as the value of $\Delta I/I$ caused by the polishing errors and density inhomogeneities.

For a rotor constructed from a homogeneous, isotropic elastic material spinning at rate, ω_G , the uncompensated gravity-gradient drift averaged around a circular orbit, $\dot{\phi}_{av}$, is given by [47, 32, 2]

$$\begin{aligned} \dot{\phi}_{av} &= \frac{3n^2}{2\omega_G} \varepsilon_T \theta_{ml} = \frac{3n^2}{2\omega_G} (\varepsilon_p + \varepsilon_{elastic}) \theta_{ml} \\ &= \frac{3n^2}{2} \left(\frac{\varepsilon_p}{\omega_G} + \frac{k_v \rho a^2}{E} \omega_G \right) \theta_{ml}. \end{aligned} \quad A1$$

θ_{ml} is the effective misalignment between the spin axis and the orbit plane or the orbit normal depending on the experiment, $\rho = 2340 \text{ kg/m}^3$ for Silicon, $a = 2.5 \text{ cm}$, and E is the Young's modulus of Silicon $= 1.7 \times 10^{11} \text{ N/m}^2$. $\varepsilon_{elastic} = k_v \rho a^2 \omega_G^2 / E$ where $k_v = (\nu + 1)(\nu + 2) / (5\nu + 7)$ and ν is Poisson's ratio $= 0.22$ for Silicon giving $k_v = 0.33$.

Equation A1 has an optimum value of ω_G which minimizes the drift rate with ε_p equal to $\varepsilon_{elastic}$

$$\omega_{G \text{ opt}} = \sqrt{\frac{\varepsilon_p E}{k_v \rho a^2}}. \quad A2$$

This value of ω_G gives a minimum gravity-gradient drift rate of

$$\dot{\phi}_{av \text{ min}} = 3n^2 a \sqrt{\frac{k_v \rho \varepsilon_p}{E}} \theta_{ml}. \quad A3$$

Equation A2 gives a rotor spin rate of 924 Hz for a 2.5-cm radius Silicon rotor with $\varepsilon_p = 10^{-4}$; and once the rotor size and material have been chosen, the gravity-gradient drift is determined only by the effective value of θ_{ml} and the square root of ε_p .

Based on Equation A3, it might be thought that the correct approach to reduce the gravity-gradient drift would be to make ε_p as small as possible. This is, however, undesirable as the optimum spin speed is also proportional to the square root of ε_p , so that a small ε_p results in a low rotor speed which increases the drifts from other torque sources such as gas brownian motion. Furthermore, a smaller ε_p only improves the drifts as $\varepsilon_p^{1/2}$ so that making it smaller than 10^{-4} does not bring a significant gain over the best spheres which can be polished ($\varepsilon_p = 10^{-6}$), only a factor of $100^{1/2} = 10$. In addition, reducing the gravity-gradient drift by making ε_p very small is also undesirable because it makes the rotor harder to manufacture and makes the measurement of the flat alignment more difficult. On the other hand, the effective value of θ_{ml} may be made so small by the proper choice of the orbit that $\varepsilon_p = 10^{-4}$ gives acceptable gravity-gradient drifts. These considerations are important since they show that it is not desirable to attempt to fabricate a gyro rotor of any better quality than $\varepsilon_p = 10^{-4}$ which is the natural value that arises with two flats ten percent of the diameter of the rotor.

Appendix A2. The Gravity-Gradient-Drift Errors

The simulation in Appendix B shows that the orbit can always be chosen to return the y -gravity-gradient-drift angle (the experiment axis) to zero at the end of the year, but a perfect orbit cannot be obtained in practice. The question then arises what is the sensitivity of the y -gravity-gradient drift to the orbit errors, and how large are these errors. In calculating these sensitivities, one can also consider the x -component of the geodetic drift; since it also depends on the orientation of the orbit plane.

For the geodetic experiment where the gyro spin vector is in the orbit plane, there are only four nonzero first-order sensitivity terms. They may be calculated to a few percent accuracy from the naïve formulas for the drifts due to orbit misalignment without taking account of all of the external disturbances from the

sun, moon, precession, nutation, the earth's real gravity field, etc. since they come from a trajectory linearized with respect to the more exact orbit. If i' is the coinclination ($90^\circ - i$), Ω is the right ascension relative to the reference star, ϕ_y is the y -component of gravity-gradient drift, and g_x is the x -component of the geodetic drift; the four non-zero sensitivities for the positive orbit are given by:

$$\frac{\partial \phi_y}{\partial i_0'} = -\dot{\phi}_{gg} t \sin \delta - \dot{\phi}_{gg} \frac{\partial \dot{\Omega}}{\partial i_0'} \frac{t^2}{2} \cos \delta, \quad A4$$

$$\frac{\partial \phi_y}{\partial \Omega_0} = -\dot{\phi}_{gg} t \cos \delta, \quad A5$$

$$\frac{\partial g_x}{\partial i_0'} = \dot{g}_{geo} t \cos \delta - \dot{g}_{geo} \frac{\partial \dot{\Omega}}{\partial i_0'} \frac{t^2}{2} \sin \delta, \quad A6$$

and

$$\frac{\partial g_x}{\partial \Omega_0} = -\dot{g}_{geo} t \sin \delta \quad A7$$

where δ is the declination of the reference star, $\dot{\phi}_{gg} \equiv 3n^2 \varepsilon_T / 2\omega_G$, and $\dot{g}_{geo} \equiv 3GM_\oplus n / 2c^2 r_s$. Table A1 shows the theoretical sensitivities with respect to the initial coinclination and relative longitude of the ascending node calculated from the above expressions for a one-year experiment as well as the average x -gravity-gradient drift angle which will be discussed below.

Table A1 shows that only $\partial \phi_y / \partial i_0'$ (or equivalently during the year, $\partial \phi_y / \partial i'$) is important; and the calculations for the compensation errors will be based only on this term. Since the orbits are chosen to drive the final value of the gravity-gradient drift to zero in the experiment axis and the final value of the geodetic drift to zero in the cross axis, it is the sensitivities which determine the y -gravity-gradient and x -geodetic drift errors.

Star	Declination (deg)	$\frac{\partial \phi_y}{\partial i_0'}$ ($\mu\text{as} / \text{''}$)	$\frac{\partial \phi_y}{\partial \Omega_0}$ ($\mu\text{as} / \text{''}$)	$\frac{\partial g_x}{\partial i_0'}$ ($\mu\text{as} / \text{''}$)	$\frac{\partial g_x}{\partial \Omega_0}$ ($\mu\text{as} / \text{''}$)	$\bar{\phi}_x$ μas
Achernar	-57.24	12.1	-0.72	-294.7	20.3	-22.2
Rigel	-8.204	20.2	-1.32	-28.4	3.44	-6.88
Capella	46.00	13.1	-0.93	280.0	-17.3	24.3
Mintaka	-0.2992	20.2	-1.33	22.2	0.126	-0.25
Alnilam	-1.202	20.2	-1.33	16.4	0.506	-1.02
Canopus	-52.70	13.3	-0.81	-276.5	19.2	-23.5
Sirius	-16.72	19.8	-1.28	-82.2	6.9	-13.4
Procyon	5.225	20.0	-1.33	57.3	-2.2	4.42
Mimosa	-59.69	11.4	-0.67	-303.8	20.8	-21.2
Hadar	-60.37	11.2	-0.66	-306.2	21.0	-20.9
Arcturus	19.18	18.7	-1.26	143.0	-7.9	15.1
δ Oct	-83.67	3.55	-0.147	-361.1	24.0	-5.34
Rigel Kent	-60.84	11.0	-0.65	-307.9	21.1	-20.7
Vega	38.78	14.9	-1.04	248.1	-15.1	23.8
Melik	-0.3197	20.2	-1.33	22.1	0.135	-0.27
Polaris	89.26	-1.07	-0.0171	366.3	-24.1	0.626

Table A1. One-Year Drift-Angle Sensitivities, 1500-km Polar Orbit

The other two components, the y -geodetic drift and the x -gravity-gradient drift, have no first-order sensitivity to the orientation of the orbit plane. Furthermore, the y -geodetic drift is the desired outcome of the experiment, and for a spherical earth the average value of the x -gravity-gradient drift is zero. This average, however,

is not exactly zero due to the presence of the J_2 term in the earth's gravitational field. It is the sum of two effects: a rectification of the twice per orbit altitude oscillations due to J_2 with the twice-orbit oscillations of the instantaneous x -gravity-gradient drift and a term stem-

ming directly from J_2 . The last column of Table A1 shows its value for the stars listed there. Since it is also desired to simultaneously measure the frame-dragging drift to high precision, $\bar{\phi}_x$ is an error term for that measurement; and it is desirable to compensate this drift. Its value is given by

$$\bar{\phi}_x = \frac{3}{16} J_2 \frac{n^2 \varepsilon_T}{\omega_G} \left(\frac{R_e}{r_s} \right)^2 \sin(2\delta). \quad \text{A8}$$

A twice-orbit oscillation of amplitude $3n\varepsilon_r/4\omega_G = 4.82 \mu\text{as}$ is superposed on the average drift angle from Equation A8. This is the term which rectifies with the J_2 -induced altitude oscillations to give part of the expression in Equation A8.

Although the physical y-gravity-gradient drift angle at the end of the experiment is determined by the deviation of the real orbit from the ideal orbit, this angle can be calculated to an accuracy which depends on the accuracy with which the orbit can be measured during the year. Compensation by calculation is standard practice for ultra-low-drift inertial-quality gyros and will also be used here to gain the last factor of approximately six

in the gyro performance. Table A2 shows the errors in this calculation and also in calculating the precise value of the geodetic drift. It will be assumed that Alnilam is the reference star, that the orbit can maintain i' within about 10 mas of the ideal orbit, and that i' can be measured to 1.5 mas which corresponds to a cross-track error of 5 cm [42]. The orbit plane errors for the y-gravity gradient can then be calculated by multiplying the value in Table A1 for $\partial\phi_y/\partial i_0'$ by 0.0015. The x-geodetic sensitivities to the orbit-plane errors are similarly calculated. The altitude errors are calculated by differentiating the drift with respect to the radius vector and multiplying by 5 cm, i.e. $\partial\phi_y/\partial i_0' \times 0.01$ is multiplied by $3 \times 5 \text{ cm} / r_s$. The rotor-spin errors assume that the gyro spin speed can be measured to one part in 10^9 . The compensation of $\Delta I/I$ assumes that the elastic bulge of the rotor can be calculated to 0.1 percent which corresponds to dividing the drift by 2000 since the permanent bulge can be measured to very high precision from the polhode period so that only half of the bulge has the 0.1 percent error. The geocentric gravitational constant, GM_\oplus , is assumed to be known to one part in 10^9 [48]; and to get its error contribution, the gravity-gradient drift is multiplied by 10^{-9} and the geodetic drift by 1.5×10^{-9} .

	Error Source	Experiment Axis (y-axis) ($\mu\text{as}/\text{yr}$)	Cross Axis (x-axis) ($\mu\text{as}/\text{yr}$)
Gravity Gradient	Orbit Plane	0.0304	
	Declination		1.02E-07
	Altitude	3.86E-09	1.30E-08
	Rotor Spin	2.02E-10	1.02E-09
	ε_p	0.0001	0.00051
	GM_\oplus uncertainty	2.02E-10	1.02E-09
	RSS	0.0304	0.00051
Geodetic	Orbit Plane		0.0246
	Altitude	0.0790	3.13E-07
	GM_\oplus uncertainty	0.0075	2.46E-08
	RSS	0.0790	0.0246

Table A2. Gravity-Gradient Compensation and Geodetic Drift Calculation

The compensated drifts in the cross-axis determine how accurately the gyro drift performance can be monitored during the experiment as well as the errors in a simultaneous frame-dragging measurement for which

the geodetic drift as well as the gravity gradient is an error source. It can be seen that the principle error in compensating the gravity-gradient drift is the tracking error.

Appendix A3. Magnetic-Eddy-Current, Barnett-Effect, and Spinning-Charge Drifts

Since the Unsupported Gyro is spun up, damped, and aligned with the reference star by means of an eddy-current induction motor, the rotor must be slightly conducting. This also eliminates the problem of charges being trapped in the interior of the rotor. A conducting rotor, however, is subject to drift due to torques from eddy currents induced in the rotor by the earth's magnetic field. Thus the rotor conductivity must be chosen to provide adequate spinup torque without causing excessive gyro drift. It turns out that (with proper shielding) this can be done. The expression for the eddy-current drift given in Table 2,

$$\dot{\phi}_{av} = \frac{\sigma B_{e\perp} B_{e\parallel} S_{AC}^2 C_M A_{orbit}}{4\rho},$$

is derived in [32]. It depends on the components of the earth's magnetic field perpendicular and parallel to the spin axis, $B_{e\perp}$ and $B_{e\parallel}$, the AC attenuation at roll frequency of the magnetic shield, S_{AC} , and the averaging from the orbit, A_{orbit} . C_M is the compensation of the eddy-current drift, if any, which might be applied. $C_M = 1$ means no compensation; and $C_M = 0.1$, for example, implies that a calculation with a 10 percent error has been used to compensate the drift. In the ideal case, the average drift would be zero [2], that is, the average of $B_{e\perp} B_{e\parallel}$ in a circular orbit around a rotating inclined dipole is zero if the gyro spin axis is parallel or perpendicular to the dipole rotation axis and parallel or perpendicular to the orbit normal. This is obvious if the dipole is parallel to the earth's rotation, but it is also true for an inclined dipole. The values in Table 2 were calculated by numerical integration of the orbit using the IGRF model (Cf. Appendix B). Because the average of the eddy-current drift is ideally zero, it is important to determine the actual drift through simulation and not from the peak values. For example with $B_e = 0.3$ gauss and $\sigma S_{AC}^2 C_M = 10^{-5}$ mhos/m, the formula for the peak eddy-current drift above gives a value of $6.3 \mu\text{as/yr}$ which is about 900 times greater than the simulation value in Table 2 for Alnilam with a declination of -1.2 deg and about 3500 times greater than the equatorial stars Mintaka and Saad el Melik. Because the drift is proportional to the square of the AC magnetic shielding and the first power of σ , the simulation may be used to study any combination of these parameters by scaling the results as σS_{AC}^2 .

In addition to the gyro drift caused by eddy currents in a conducting rotor, there are two other magnetic drift sources which arise because the rotor spin causes it to have a magnetic moment. One is the Barnett effect and the other is spinning charge on the rotor. Both of these drifts go as the first power of the shielding and eventually come to dominate the magnetic drifts as the shielding improves. The Barnett effect is due to the fact that rotating a material body causes the electron spin and orbital angular momenta to attempt to line up with the rotation axis so that by the gyromagnetic theorem, rotor spin induces a magnetic moment, \mathbf{m}_H , in a solid body. This moment is given by

$$\mathbf{m}_H = \frac{2V_{ol} \chi_m}{\mu_0 g_m e/m_e} \boldsymbol{\omega}_G \quad \text{A9}$$

where V_{ol} the volume of the rotor, χ_m the magnetic susceptibility, μ_0 the permeability of free space, g_m the g -factor for the gyromagnetic ratio of the bulk material, and e/m_e the electron charge to mass ratio. This magnetic moment interacts with the ambient magnetic field to produce a mechanical moment which causes a gyro drift proportional to the magnetic field.

The spinning-charge drift is caused by the fact that a spinning charged rotor generates circulating currents with a magnetic moment given by

$$\mathbf{m}_H = \epsilon_0 V(1 + a/d) V_{ol} \boldsymbol{\omega}_G \quad \text{A10}$$

where V is the potential due to the charge on the rotor. The factor $(1 + a/d)$ arises because the cavity shield with gap, d , increases the effective capacitance of the rotor. The spinning-charge drift has exactly the same form as the Barnett drift and can be obtained by multiplying the results of the Barnett simulations by a numerical factor,

$$\begin{aligned} \dot{\phi}_{sp\ chg} &= \frac{g_m eV(1 + a/d)}{2 m_e c^2 \chi_m} \dot{\phi}_{Barnett} \\ &= -0.920 \left(\frac{V}{1 \text{ volt}} \right) \dot{\phi}_{Barnett} \end{aligned} \quad \text{A11}$$

The requirement on any residual constant field inside of the magnetic shield is much less severe than for AC fields such as \mathbf{B}_e . This is because any constant magnetic fields arising from the satellite are roll aver-

aged by the satellite's spin, and magnetic fields from currents at roll frequency such as from the solar panels can be designed to be smaller than the earth's field. An internal satellite-fixed field would arise because mumetal shields also typically have a small constant residual magnetic field inside of the shield due to magnetization of the shield itself. It is important to estimate how well roll averaging and the magnetic shield eliminate drifts caused by constant magnetic fields internal to the satellite. For this calculation, the inertially fixed component of satellite attitude misalignment with respect to the gyro, ϵ_{Att} , will be taken as 10^{-8} radians or about 2 mas attitude error. (ϵ_{Att} is used instead of the ef-

fective roll averaging, A , because the rotor cavity position plays no roll in this calculation since the product of $B_i \Delta B_i$ where ΔB_i is the change due to the field gradient is much smaller than B_i^2). Gyro drift from this source would then arise because the spin down torque caused by the angular velocity of the rotating magnetic field seen by the rotor, which is the difference between the gyro spin rate and the satellite spin rate, is misaligned due to this angle. For $\epsilon_{Att} = 10^{-8}$ rad and a drift requirement of $0.006 \mu\text{as/yr}$, this effect sets a limit on a residual field of $0.3 \times 10^{-3} \text{ Gauss} = 3 \times 10^{-8} \text{ Tesla}$, i.e. about 1000 times smaller than the earth's field.

$7 \times 10^{-3} \mu\text{as/yr}$	Conductivity, σ mhos/meter	Shielding, S_{AC}	Compensation, C_M	$\sigma S_{AC}^2 C_M$ mhos/meter
Baseline	10^5	10^{-5}	1	10^{-5}
Backup 1	10^3	10^{-4}	1	10^{-5}
Backup 2	10^4	10^{-4}	0.1	10^{-5}

Table A3. Conductivity, Attenuation, Compensation Combinations

The magnetic shield is a sphere with an outer diameter of 25 cm consisting of four or more layers of one-mm mumetal spaced one cm apart with an initial permeability of 120,000 and a maximum permeability of 350,000. The drift specification requires that the combination $\sigma S_{AC}^2 C_M$ be less than 10^{-5} mhos/meter for an eddy current drift of $7 \times 10^{-3} \mu\text{as/yr}$ for Alnilam. The requirement is expressed in this form because the exact degree of shielding which can be obtained is controversial⁹. Table A3 shows example of various combinations which can fulfill the drift requirements.

Appendix A4. Roll Averaging

The gyro drifts can be greatly reduced by roll averaging the satellite-fixed disturbing torques. The precision with which roll averaging can be maintained depends on the accuracy with which the drag-free control system can keep the rotor inertially centered in the cavity, the accuracy with which the satellite attitude con-

trol system can hold the inertial component of the spin axis of the satellite aligned with the spin axis of the gyro, and the number of roll cycles.

These accuracies depend on the noise in the pickup systems, the disturbing forces and torques, the alignment of the center of mass of the satellite with the center of the cavity, and the alignment of the maximum moment-of-inertia axis with the zero point of the autocollimator. The requisite alignments are maintained by the automatic mass trim system which is the baseline for the GP-B experiment and for the experiment described here [49]. The remaining errors in the mass trim system are absorbed by the zero-point adjustment in the autocollimators and transcollimators and by the drag-free position and satellite attitude control systems. In this paper it is assumed that roll averaging, A , can be maintained to 10^{-7} . With a one-cm gap this sets a requirement of 10^{-9} meters on the inertial component of position error and a requirement of 10^{-7} radians, i.e. 20 mas, on the inertial component of misalignment between the gyro and the satellite spin axes. Since inertial errors show up in the satellite as roll-frequency errors, this performance is maintained among other things by a roll-frequency pole in both the drag-free and attitude feedback loops. This plays the same role at roll frequency that the integrator in a PID system plays at DC. Theoretical calculations and simulations by the author and the scaling of simulations for the GP-B satellite show that this performance can be achieved given the predicted noise in the translation and attitude sensors, about $1.2 \times 10^{-10} \text{ m/Hz}^{1/2}$ for the transcollimator and

⁹ Two shield manufacturers, Vacuumschmelze and Mu Shields, claim that they can furnish flight qualified multilayer shields with an AC attenuation of 3×10^{-6} or even 10^{-7} , but two GPB team members with considerable experience in magnetic shielding claim that reliable attenuation better than 10^{-4} is not possible.

8 $\mu\text{as}/\text{Hz}^{1/2}$ for the autocollimator. RMS following errors of a few mas are predicted for the GP-B attitude control; and given the increased gyroscopic stiffness of the AC-USG satellite and the much lower noise of the attitude sensor, it is expected that attitude control to less than one mas will be possible. This corresponds to a roll averaging error due to the attitude control of less than 10^{-8} .

In addition to cavity miscentering and attitude errors, the accuracy of roll averaging is determined by the number of cycles over which an error is averaged. This is due to the fact that the error induced in the first half roll cycle is never recovered. When a gyro drift torque is integrated to give the drift angle, one of the roll averaged components is proportional to $1 - c\omega_R t$ which has an average value of one not zero. To dominate this error, the number of revolutions must exceed $1/2 \pi A$. This requires that the roll period be shorter than $2\pi A t$, or less than about 19 seconds for a one-year experiment with $A = 10^{-7}$.

Appendix A5. Gas Brownian Motion and Gas Spin-Down Drifts

Even at pressures between 10^{-7} and 10^{-9} Torr, there are a very large number of gas molecules in the cavity, about 3×10^{17} molecules per cubic centimeter at 10^{-9} Torr and 300 K. In addition, at 300 kelvins there are roughly 55×10^{17} photons per cubic centimeter. The gas molecules and photons cause the gyro to drift because they apply a misaligned spin-down torque, and they cause the spin axis to random walk away from its initial direction proportional to the square root of time. The gas and photon spin-down drag and the Brownian "drift" are calculated in [2] which gives a detailed derivation of the formulas for the gas and photon torque coefficients and the Brownian drift.

The formula for the random walk of the spin axis or Brownian drift is the same for gas molecules and for photons; only the expressions for the torque coefficients are different. The gas or the photons cause a spin-down torque which is given by

$$M_{SD} = -b\omega_G - b_2\omega_G^2 \quad \text{A12}$$

with $b_2 = 0$ for photons. For b_2 negligible, the random walk of the gyro spin axis is

$$\langle \phi^2 \rangle = \frac{4bkTt}{h_G^2} \quad \text{A13}$$

where k is the Boltzmann constant, T the absolute temperature in kelvins, h_G the gyro angular momentum, and ϕ the angular random walk of the spin axis with time. The linear torque coefficient for gas molecules is given by

$$b_{Gas} = \frac{8\pi}{3} a^4 p \sqrt{\frac{m_a}{2\pi kT}} \quad \text{A14}$$

where p is the gas pressure in the cavity and m_{av} is the average molecular mass of the gas. For photons, b_{ph} is given by

$$\begin{aligned} b_{ph} &= \frac{32}{5} \left(\frac{\pi}{3}\right)^2 \left(\frac{\pi}{K}\right)^4 \left(\frac{a}{\lambda_m}\right)^4 h \\ &= 1.11249 \left(\frac{a}{\lambda_m}\right)^4 h \end{aligned} \quad \text{A15}$$

where the peak wave length of the black-body radiation in the cavity, $\lambda_m = hc / KkT$ with $K = 4.9651$. The photon drifts are negligible since the photon drag gives a spin-down time constant of about 36 million years.

The gas spin-down drift is caused by the fact that the nonsphericity of the satellite cavity causes the drag torque to be slightly misaligned from the gyro spin axis. This misalignment is quantized by ϵ_{ml} , i.e. the spin-down torque perpendicular to the spin axis is given by the spin-down torque times ϵ_{ml} . Because the calculation of ϵ_{ml} is difficult, it has been estimated. It is important to make this estimate as correctly as possible. Too high an estimate can place an unrealistic requirement on the allowable cavity pressure. Too low an estimate can result in neglecting an important drift source. Two extremes can be identified. A lower bound is the cavity sphericity attenuated by the one-cm gap, about 10^{-6} . On the other hand 0.01 or even 0.001 seem much too large. Thus ϵ_{ml} probably lies between 10^{-4} and 10^{-5} . Conservatively, 10^{-4} will be used. The gyro drift due to spin-down misalignment is then given by the spin-down torque times the roll averaging, A , times ϵ_{ml} divided by the gyro angular momentum.

With a cavity pressure of 10^{-9} Torr the gas spin-down time constant is about 3170 years giving a gas spin-down drift of 0.0064 $\mu\text{as}/\text{yr}$. It is clear that the cav-

ity pressure need not be 10^{-9} Torr; it could be 10^{-8} , or with ϵ_{ml} equal to 10^{-5} , even 10^{-7} Torr would give acceptable drifts. 10^{-9} Torr, however, is attainable with care as can be seen from the following considerations: Extrapolating the gas pressure and scale height at one thousand km in the 1976 atmosphere [50], the outside pressure at 1500 km is found to be about 2×10^{-11} Torr which could rise to 10^{-9} Torr at a solar maximum. The pressure from the drag-free thruster exhaust can be estimated from the flow necessary to balance the solar radiation pressure and is roughly 3×10^{-12} Torr. The external pressure can be drastically reduced by proper design of the spacecraft exhaust ports so that they always exhaust behind the vehicle. Thus the cavity pressure is determined only by outgassing, and the proper choice of materials plus baking combined with the approximately one-year wait to establish the counter-rotating orbits could achieve a cavity pressure of 10^{-9} Torr. Since the gas brownian drift increases as the square root of the pressure, however, it could be as much as two orders of magnitude greater, (10^{-7} Torr) before the gyro drift was significantly affected..

Appendix A6. Rotor Collisions with Large Particles in the Cavity

The existence of large particles in the cavity which could collide with the rotor is a possible problem for the design of the relativity gyro. It is mandatory that the cavity environment be as clean as possible, but the gyro also has a natural mechanism for eliminating particles. Large particles do not bounce back and forth and continue to collide with the rotor indefinitely; they be-

come trapped. This is what in clean-room terminology is called the "quiescent state" which means that although there may be tens or hundreds of thousands of particles present, unless they are somehow stirred up, they are all caught in various "trapping sites" in the cavity and in the vacuum exhaust lines. The particles will be swept out of the cavity space by the spin of the rotor with a time constant of less than a second because continual collisions eventually bring every particle to a site where it is trapped. This effect is helped by the spin of the satellite which, for example, at one radian per second gives an artificial gravity of roughly 0.005 g at a radius of 3.5 cm. This and the roughly 10,000-g specific adherence forces should be compared with the disturbing specific forces which are of the order of 10^{-9} g's. The particle count requirements for the cavity may be estimated by calculating the maximum angular momentum change which could occur in the rotor for a 0.5- μ size particle, and then calculating the corresponding spin angle change. 0.5- μ is used because in general larger particles can be removed at final assembly, and particles smaller than 0.5 μ quickly adhere very strongly to the neighboring surfaces. The "drift" is a random-walk process so that the total angle change is proportional to the square root of the number of collisions, and Table A4 shows that no more than 3700 collisions can be tolerated. Once the experiment is begun, however, the satellite experiences no shocks to stir up the particles; and no collisions are expected after the first few seconds of gyro operation. A different problem, a jam in the gap from a very large particle is impossible since the gap is very wide, one cm; and unlike an ESG with a very small gap, this cannot happen.

"Drift" in One Year (μ as)	Number of Particle Collisions per Year
10	3.67E+07
1.0	3.67E+05
0.1	3673
0.01	37

Table A4. The Effect of 0.5-Micron-Diameter Particles in the Cavity

Appendix A7. Flat Differential Pressure

At least in the early stages of the mission, the cavity will continually outgas, and the molecules will be removed by the vacuum exhaust system. This constitutes a current which applies a force to the rotor. The resulting gyro drift may be bounded by assuming that the full cavity pressure acts on only one miscentered flat or on only one side of a spherical rotor with a slight

error between the geometrical center and the center of mass.

Appendix A8. Electric Fields in the Cavity

Because of the large gap, electric fields which could cause gyro drift come only from rotor charge. It is sufficient to bound these drifts, and this is done by multiplying the total force from the electric field times the

rotor radius times a nonsphericity, misalignment, or mis-centering parameter. The electric drifts in Table 2 were calculated with the assumption that the charge can be controlled so the rotor charge potential is less than 10 volts.

Appendix B. Zero-Gravity-Gradient Orbits

Modern satellite tracking systems using GPS and laser ranging can determine the position of a satellite to about 5 cm in altitude and cross track [42]. This corresponds to an angle error of about 1.5 mas for the orientation of the orbit plane. It is possible to take advantage of this capability to fine tune the orbit of a drag-free satellite to materially reduce the y -gravity-gradient and x -geodetic drift. If the magnetic drifts are also calculated for the orbit, it is possible to see how much orbit averaging is present with the real magnetic field of the earth which, of course, does not exactly satisfy the conditions for the orbit average to be zero.

This section describes an orbital simulation for two satellites in counter-rotating polar orbits at 1500 km. It includes the perturbations of the earth's zonal and tesseral harmonics up through degree four, the sun, the moon, the precession of the equinoxes, and the earth's nutation. It is written in Fortran, and there are 40 state variables with 1,052,000 integration steps of 30 seconds each. The equations of motion of the earth and moon and two satellites as well as the relativity-geodetic, gravity-gradient, eddy-current, and Barnett drifts for two satellites are integrated in a heliocentric J2000 inertial reference with the sun assumed to be stationary. The earth's harmonics are taken from the joint University of Texas/Goddard JGM gravity model, and the magnetic field is the International-Geomagnetic-Reference-Field (IGRF) spherical-harmonic model carried to degree four which gives a magnetic-field accuracy of approximately one percent. The simulation begins at J2000.0 since it was relatively easy to obtain the heliocentric initial conditions for the earth and the moon at this time which were furnished by Miles Standish of JPL [41]. Since the purpose of the simulation is to establish the feasibility of the method and to see whether any practical considerations such as the precession of the equinoxes or the moon's perturbations would destroy the precision cancellation of the gravity-gradient angle, the accuracy of the perturbations is not carried to the degree which would be used in an operational simulation for the actual experiment itself. For example, only the first two terms in the nutation series are included so that the error of the earth's spin axis is of the order of a few tenths of an arcsec. Although the only odd harmonic included in the simulation is J_3 , its value has been artificially increased from 2.53×10^{-6} to 2.94×10^{-6} so that the initial

eccentricity would give the correct value for a "frozen orbit" with the first 17 odd zonals.

Although the equations are solved in J2000, the gyro drift results are presented in the star reference frame with the z -axis parallel to the gyro spin axis (almost exactly pointing at the reference star) and the x -axis making the smallest possible angle with respect to the earth's north pole. The y -axis geodetic drift is the desired measurement, and the x -axis is the cross axis. Since the x -geodetic drift and the y -gravity-gradient drift are affected by the orientation of the orbit plane, the tuning of the orbit is accomplished by selecting the initial coinclination (inclination relative to z_j or the north pole) and longitude of the ascending node. The P orbit's angular momentum is parallel to the y -axis, and the N orbit is its counter-rotating partner.

Figures B1 and B2 show coinclination, i' , and longitude of the ascending node, Ω , relative to Alnilam as the reference star. The coinclination is chosen so that the average of the longitude of the ascending node relative to Alnilam is approximately zero which causes the y -gravity-gradient drift and the x -geodetic-relativity drift to first grow and then return to zero at the end of the year as can be seen in Figures B3 and B4. The coinclination is shown both for the positive (P) and negative (N) satellites and both relative to J2000 and relative to the true earth of date (TOD). The curves relative to J2000 lie on top of each other and cannot be distinguished in the plots. The coinclinations relative to the earth slowly diverge from the middle curve mostly due to the precession of the equinoxes. It can be seen that the average of the coinclination relative to J2000 is approximately zero. In both Figures B1 and B2 the six-month period of the perturbation of the sun can be clearly seen; and in Figure B1, the two-week period of the perturbation of the moon is discernible. The two-week lunar period is also present in the longitude curves, but it is weaker.

The initial coinclination and relative longitude were chosen to also zero the x -geodetic drift because although a precision frame-dragging measurement would normally be done in a separate experiment, it is still desirable to measure frame dragging simultaneously with the geodetic drift; and the x -axis is the experiment axis for frame dragging. Since the amplitude of the geodetic term can be approximately 160 times as big as frame dragging, it could be a significant error. At any rate there is no other reasonable choice since both the x -gravity-gradient and y -geodetic drifts are not affected to first order by the orientation of the orbit plane .

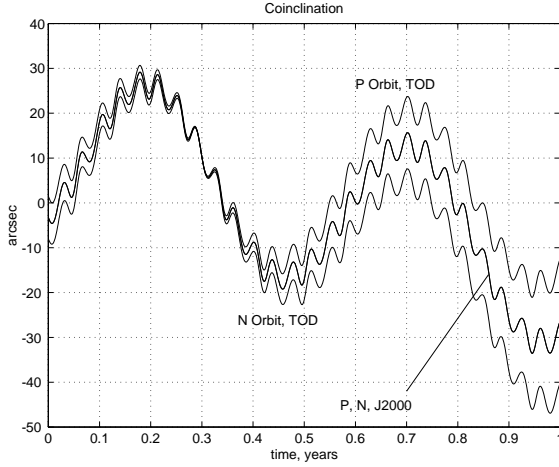


Figure B1. Coinclination

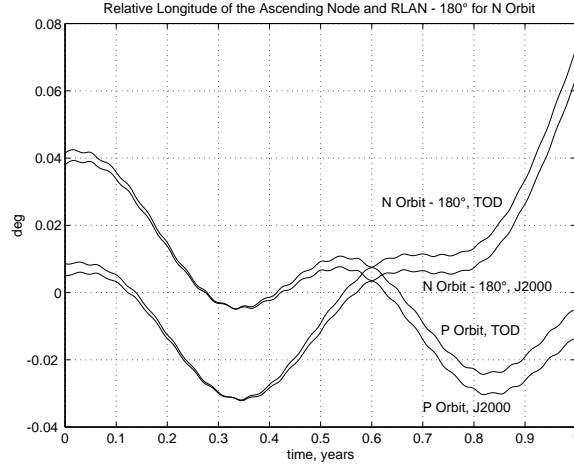
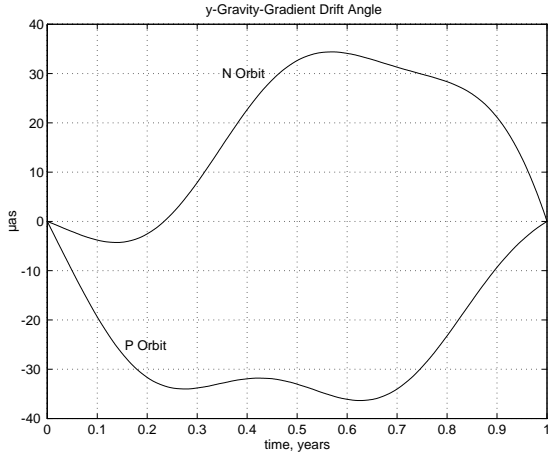

 Figure B2. Relative Ω


Figure B3. y-Gravity-Gradient Angle

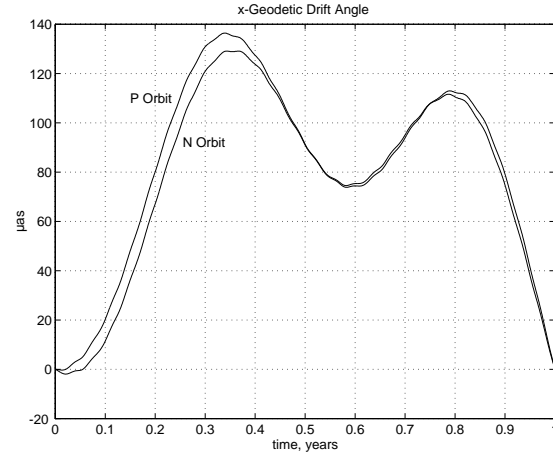


Figure B4. x-Geodetic Drift Angle

Because of the orbit averaging discussed in Appendix A3, the magnetic drifts must be determined from the simulation. If $\dot{\phi}_{xe}$, $\dot{\phi}_{ye}$, and $\dot{\phi}_{xb}$ are the x -eddy-current, y -eddy-current, and x -Barnett drifts respectively; the results of the simulations for seven stars with declinations from 40 to -60 deg with a satellite altitude of 1500 km, $\sigma = 10^5$, $S_{AC} = 10^{-5}$, and the IGRF magnetic field can be accurately fitted with the following expressions:

$$\dot{\phi}_{xe} = 0.73 \times 10^{-2} \mu\text{as/yr} \cos \delta,$$

$$\dot{\phi}_{ye} = 16.7 \times 10^{-2} \mu\text{as/yr} \sin 2\delta,$$

and

$$\dot{\phi}_{xb} = -2.9 \times 10^{-2} \mu\text{as/yr} \cos 2\delta$$

where δ is the declination of the star. The working of the orbit averaging can be seen here. $\dot{\phi}_{xe}$, would be zero for a dipole with zero offset, and it is thus much smaller than $\dot{\phi}_{ye}$, since it depends on the non-dipole terms in the field. Likewise, the $\sin 2\delta$ term in the expression for $\dot{\phi}_{ye}$, is zero at the equator or at the poles. The y -component of the Barnett drift is not shown, because it is not a drift but rather has a diurnally oscillating value of about $1.3 \times 10^{-6} \mu\text{as}$ on top of a constant term of the same size.

Appendix C. Autocollimator Performance

In order to determine the performance of the autocollimator as a gyro readout, there are three items to

check: the instrument noise equivalent angle, the zero point errors, and the scale factor errors.

Appendix C1. Autocollimator Noise Equivalent Angle

The autocollimator noise depends primarily on the number of photons/sec in the beam and the size of the focused light spot or slit which in turn depend on the

design of the field-stop reticule. The performance reported by Jones for his optical lever [36], $14\text{-}\mu\text{s/yr}$, was achieved by having a large number of photons combined with a small effective slit size. For example to divide the image of the focused slit by 3×10^6 in one second in the presence of photon shot noise, approximately 10^{13} photons are needed. This is converted to an angle by dividing by the focal length; and if the focal length is about 3×10^3 times the slit size, this gives 10^{-10} radians or about $20 \mu\text{as}$.

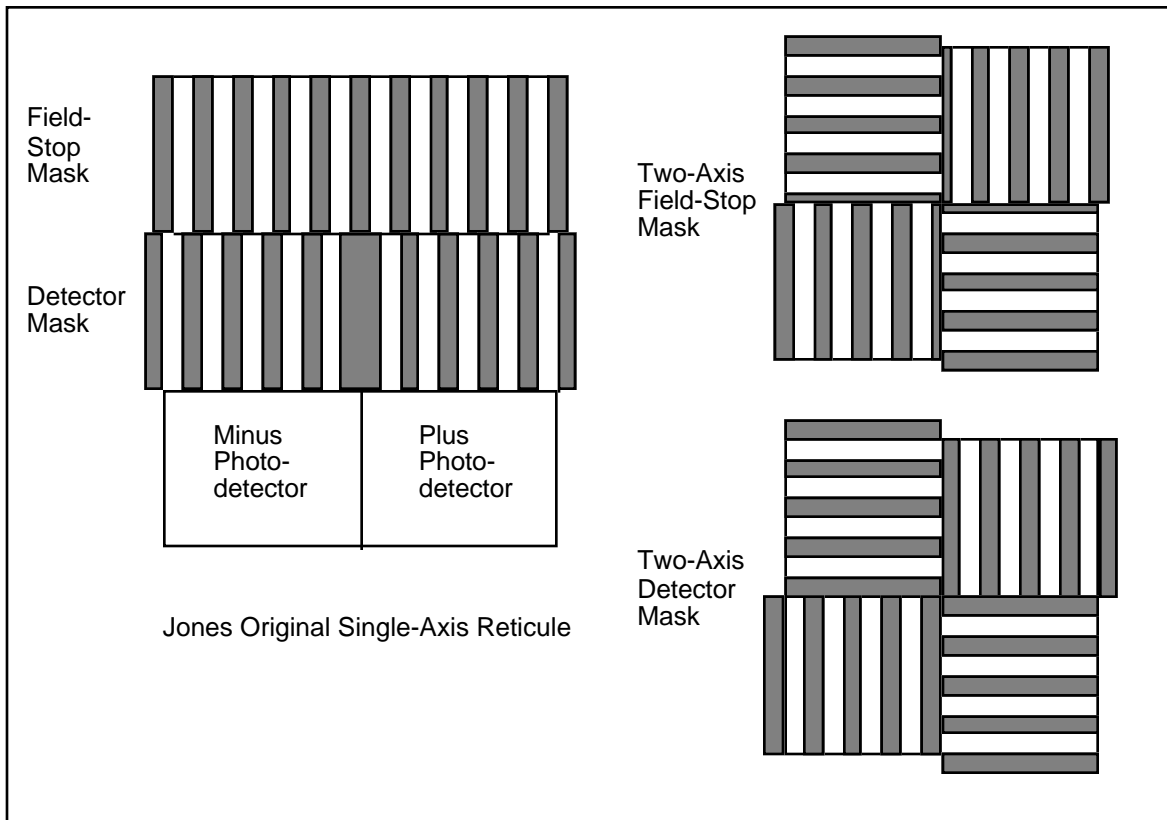


Figure C1. Single- and Two-Axis Jones-Pfund Type Reticules

The Jones design uses a grid of slits as shown in Figure C1 to greatly increase the amount of light in the beam while maintaining a very narrow slit and smoothing out variations in the grid and photodetector. The field-stop mask is placed at the focal point of the collimating lens next to the condensing lens in Figure 3, and the detector is masked with an identical mask except that the bars in the mask are displaced one half of the slit width (Cf. Figure C1). When the image of the field-stop mask moves in a given direction, it uncovers the detector mask on one photodetector and covers it on the other. Subtraction then generates a sig-

nal proportional to the displacement of the image of the field stop, i.e. proportion to the mirror rotation. The condenser lens focuses the image of the light source into the interior of the collimating lens thus maximally defocusing the light source and guaranteeing a very uniform intensity across the detector surface as well as capturing most of the light which passes through the collector lens. Alternately the image of the light source may be focused on the optical flat, and this captures all of the light which passes through the collector lens at the cost of some uniformity across the detector surface.

The extension of the Jones' reticule to a two-axis autocollimator is also shown in Figure C1. The noise equivalent angle in radians/Hz^{1/2} of a two-axis instrument with this reticule is given by $w/2fn^{1/2}$ where n is the total number of detected photons in all four detectors, w is the width of one slit, and f is the focal length. If L is the length of the two-axis slits, the light-transmitting area is given by $2L^2$ and is independent of w , so that the noise equivalent angle is minimized by minimizing w/f . This is in stark contrast to autocollimators with a single square hole such as the ones that Ken Lorell and David Klinger built in our laboratories in the late 1960s [49, 51]. (In their case, since n is proportional to w^2 for a given illumination, w cancels in the numerator and denominator.) The minimum value of w/f in the Jones design is limited by the diffraction of the collimating lens; or in the case of the gyro readout, by the diameter of the optical flat, d_f . In order to determine w/f , the diffraction pattern of the image of the field-stop reticule in the image plane must be computed. Since the field-stop reticule is not self luminous, the light will be at least partially coherent. To account for this, the diffraction has been computed for two cases, incoherent illumination and completely coherent illumination. For a flat diameter, d_f , of 5 mm, a focal length of 10 cm, and 0.5-micron light, $1.2 \lambda_f/d_f$ is about 12μ ; and this provides a lower limit to the slit width. The surprising result is that the slits do not need to be very much wider than this limit. For example, when the diffraction calculation is done for a slit width of 25 microns for incoherent light, the dark strip attenuates the light by 2.5×10^{-2} at the center. For completely coherent illumination, the intensity alternates in the masked region with peaks and zeros with a period of about 2.5 microns; and the attenuation at the central peak is about 2×10^{-3} . Also since the first zero of the coherent pattern is about two microns past the edge, the edge is much sharper for the coherent light as was first shown by Abbe. In either case the effect of the diffracted light on the expression for the noise equivalent angle or on the scale factor of the instrument is small, and a slit width of 25 microns is acceptable. Coherent illumination always has a much smaller value at the center of the mask; and with a fiber-optic bundle as the light source, coherent light will be possible so that the attenuation of 2×10^{-3} should be regarded as more nearly correct. If a quarter section of the reticule is assumed to be 5 mm on a side, there will be 100 grid lines in each section; and the maximum off axis angle of the $f20$ optical system will be 2.9 deg.

With $w = 25 \mu$ and a focal length of 10 cm, $w/f = 2.5 \times 10^{-4}$; and for a total number of detected photons of 10^{13} per second, the noise equivalent angle for each axis given by the above expression is $8.2 \mu\text{as}/\text{Hz}^{1/2}$. The total beam intensity of 10^{13} photons/sec corresponds to a photocurrent of $0.4 \mu\text{A}$

in each of the four detectors making almost any photodiode detected-photon-noise limited. In one axis, the shot noise from $0.8 \mu\text{A}$ is $500 \text{ fA}/\text{Hz}^{1/2}$; and this should be compared with: 1) the Johnson noise current from the 10-M to 100-G feedback resistors of the operational amplifier in the transconductance mode or the 10-M current-source resistor which is 0.4 to $40 \text{ fA}/\text{Hz}^{1/2}$, 2) the noise current of typical FET or JFET operational amplifiers which lies between $0.4 \text{ fA}/\text{Hz}^{1/2}$ and $10 \text{ fA}/\text{Hz}^{1/2}$, and 3) the shot noise from a photodiode with a dark current of 3 nA which is $30 \text{ fA}/\text{Hz}^{1/2}$. The $1/f$ corners of the detectors and amplifiers typically lie between 2 and 200 Hz so that 10- to 100-kHz chopping which any case is necessary to eliminate cross talk from stray light among the four instruments (two autocollimators and two transcollimators) completely eliminates $1/f$ noise.

Since an angle change at the mirror is multiplied by two at the photodetectors, the maximum linear range of the autocollimator is given by $w/4f = 6 \times 10^{-4} \text{ rad} = 13 \text{ arcsec}$. The maximum angle which the autocollimator must measure is about 0.2 arcsec arising from the flat misalignment error. This is one 60th of the maximum linear range and corresponds to an oscillating reticule-image motion of 0.2 microns. 13 arcsec gives a ratio of about 10^6 between the maximum linear range and the smallest angle change which can be measured with one second of averaging. This large ratio is particularly useful as it allows the zero to be set electronically with a DC current source over a wide range of misalignment of the satellite maximum axis of inertia. The DC gain at the input of the operational amplifier is $2nef/w$, about $62 \text{ pA}/\text{mas}$; so that the highest DC output gain is $6 \text{ volts}/\text{mas}$. From the input gain, the $0.5 \text{ pA}/\text{Hz}^{1/2}$ shot noise from two photodiodes corresponds to $8.1 \mu\text{as}/\text{Hz}^{1/2}$ which agrees with the noise equivalent angle calculated above. Jones also had very large effective photo currents, and this explains why he was able to operate at the photon-noise limit with very primitive detectors and electronics.

Appendix C2. Autocollimator Zero-Point Errors

The zero-point errors and drift of the mechanics, photodetectors, and electronics are removed by spinning the satellite, and this is discussed in more detail in Section 5 and Appendix F. In order to stay in each other's linear ranges and to be consistent with the flat position errors, the two autocollimators should be aligned within about one arcsec of each other. The satellite maximum axis of inertia should also be aligned to the autocollimator zero points to this tolerance, and this is accomplished with a satellite active mass-trim system [49]. The electronic zero can be set to bring the balance of any DC offsets to less than one mas, and it is the mass-trim system plus the electronic offset control

which guarantee that the largest autocollimator signals will come from the flat misalignment error and the satellite attitude motion.

Although the absolute zero-point drift in the autocollimator is removed by the satellite spin, it is still interesting to calculate what its value would be. It is determined principally by the thermal temperature coefficient of the materials and is of the order of 5×10^{-7} rad/K/meter = 100 mas/K/meter. The electronic offset drift with FET or JFET operational amplifiers is much smaller, of the order of 200 μ as/K; and even bipolar operational amplifiers give an electronic offset of about 8 mas/K. With absolute temperature control to 0.1 K and a typical autocollimator size of 0.1 meter, the absolute zero point drift is not expected to exceed one mas.

Appendix C3. Autocollimator Scale-Factor Errors

Since the satellite attitude will be controlled to the gyro and not the star, the gyro readout signals will be of the order of the satellite attitude errors. In order to achieve the smallest scale-factor errors, it is necessary that the signal currents from the gyro readout not be swamped by the much larger photodiode and flat-misalignment-error currents (Cf. Table 3). Figure C2 shows how this is done. It is a diagram of the input stage to the autocollimator electronics with typical input current levels assuming 2.5×10^{12} detected photons/sec per detector, an input gain of 62 pA/mas, a flat error of 0.1 arcsec, and a satellite attitude error of one mas.

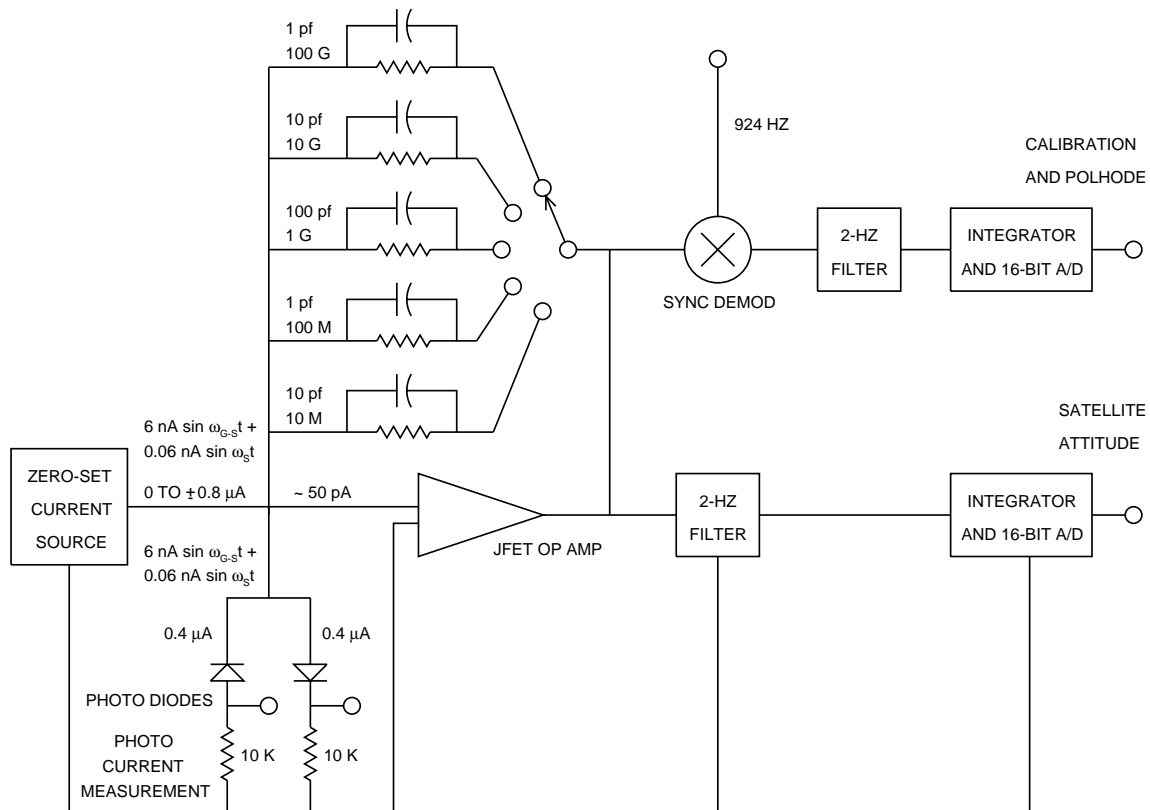


Figure C2. Autocollimator Detector Circuit

The photodiodes are hooked up antiparallel so that their 400-nA photocurrents subtract before the input to the operational amplifier; and then with proper balance from the DC current source, the only signals which flow through the feedback networks are the 6-nA currents at 924 Hz due to the approximately 0.1 arcsec flat

and/or polhode errors and the roughly 0.06-nA currents from the satellite attitude motion. The cutoff frequency of the three largest resistor networks, however, is 1.6 Hz; so that the 6-nA, 924-Hz currents flow harmlessly through their feedback capacitors only generating an output of about one volt at the highest

gain compared to 6 volts from the low frequency 0.06-nA current. This means that the 400-nA and 6-nA currents do not coexist in an amplifier with the 0.06-nA attitude signal creating dynamic-range and linearity problems. One volt, however, is large enough to still provide a useful gain-stabilizing or calibration signal since the high stability of the capacitors and the gyro spin frequency combined with accurate measurement of the satellite roll frequency allows stable operation on the descending slope of the frequency response curve beyond the feedback network's cutoff frequency. At the lower gains, however, the 10- and 100-M networks have a cutoff frequency of 1600 Hz which allows the flat-misalignment signal to be seen at its full amplitude if desired. Once the flat misalignment error has been measured with respect to the orbital aberration to a fraction of a μas ; flat-misalignment which is stable to well over 10^{-7} can take over from the aberration of starlight and provide continuous autocollimator calibration throughout the rest of the mission. The two 10-K resistors on the ground side of the photodiodes provide a continuous measurement of the photocurrent and allow possible variations in the light level to be compensated. The output of the operational amplifier is synchronously demodulated at the rotor-minus-satellite frequency of 924 Hz to recover the calibration and polhode signals. The satellite attitude and zero-point error signals are contained in the low frequency output of the operational amplifier; and the satellite attitude is subtracted from the telescope signal to eliminate satellite motion from the star-gyro angle. The gain resistors must be switchable to allow the autocollimator to operate at maximum linear range for initial acquisition.

To achieve an accuracy of a fraction of a μas , the scale factors must be calibrated to this accuracy. In the case of the autocollimator this is not particularly critical. Since the 924-Hz flat-misalignment and polhode errors can be filtered away, the largest signal in the autocollimator is due to the satellite attitude motion and is of the order of one mas. A calibration accuracy of 10^{-4} gives a final error of approximately 0.1 μas , and even a calibration as poor as one part in 10^3 would only give an error of about one μas . One problem is the photodiodes whose gain stability with respect to temperature is relatively poor, about $10^{-3}/\text{K}$; but with ten percent matching and temperature control to 0.1 K, they more than meet a requirement of 10^{-4} . Furthermore, the flat misalignment error will allow the autocollimator to stay in calibration at all future times.

Because an accuracy for the autocollimator of 10^{-4} would be acceptable, most of the calibration can be done on the ground before the flight. The principal problem is the accuracy with which the reticule lines can be laid down, approximately 0.1 μ . Reticule errors are ameliorated by the square root of the number of reticule lines and by about another factor of 10 by the continuity

of the marking process and the smearing of the image due to the diffraction of light and the optical aberrations. The telescope and autocollimator calibrations are closely connected, and the details of the calibration are discussed in Appendix G.

Appendix C4. Transcollimator

A transcollimator is an autocollimator with only one minor change. The focal length of the collimating lens is shortened so that the exit beam is focused to a point at the place where the center of the spherical gyro rotor would lie. When this is done, a translation, x , of the rotor perpendicular to the beam causes an equivalent rotation of, $\phi = x/a$. This has the advantage that almost all of the technology of autocollimators can be carried over with very little change, and it allows a precision optical measurement of rotor position with a wide gap [1, 52]. Thus with a focal length of the collimating lens such that the effective lever arm is 3 cm when reflected from the sphere and a Jones reticule with $w = 1000 \mu$, the transcollimator noise equivalent translation will be 1.2×10^{-10} meter/Hz^{1/2} with a maximum linear range of 200 μ for a rotor radius of 2.5 cm.

Within the accuracy with which the mass-trim system can center the center of mass of the satellite and with which the drag-free control system can control the satellite, the transcollimators operate with no disturbance or offset signals so that scale factor errors are not a serious problem. In addition, there is no high-accuracy requirement for the measurement of the absolute cavity position of the rotor. The only high precision requirement is that the inertial component of x - y translation be stable to 10^{-9} meters (See Appendix A4).

Appendix D. Summary of the Technique for Placing the Optical Flats on the Rotor

Polishing optical flats onto the rotor with an error of 0.1 to 0.2 arcsec with respect to the zero- g maximum axis of inertia is mostly a measurement problem. The basic method is to find the natural maximum axis of a newly polished sphere, polish an initial set of flats perpendicular to this axis, measure the error of these flats, and iteratively repolish the flats until the desired accuracy is obtained. The initial steps can be done in an air bearing to an accuracy of a few arcseconds, but the final high precision measurements must be done in an electric bearing mounted on a three axis table which tracks the spin axis of the rotor so that no torques need be applied to keep the spin axis in the field of view of the autocollimators during the precision measurement. The techniques described here were worked out between 1966 and 1972 [53, 54, 55, 33, 49].

The initial flats must be polished at the natural maximum axis of a new sphere because although the flats would determine the maximum axis of inertia on a perfect sphere, the initial moment-of-inertia difference ratio caused by surface irregularities and bulk inhomogeneity of the material would compete with the maximum axis caused by the flats to generate very large errors. If ε_{pi} is the initial permanent moment-of-inertia difference ratio of a newly polished rotor and ε_{pn} is the new value after the flats are on the rotor, the error angle between the apparent and zero-g maximum axes is given by $(\varepsilon_{pi} / \varepsilon_{pn}) \sin \theta \cos \theta$ where θ is the angle between the initial and new maximum axes. If $\varepsilon_{pi} = 10^{-6}$ and $\varepsilon_{pn} = 15(d_f / d_r)^4 / 16 \approx 10^{-4}$, the error could be as large as 0.005 radians \approx 1000 arcsec since $\varepsilon_{pi} / \varepsilon_{pn} = 10^{-2}$. In order to reduce this initial error to about 30 arcsec where it can easily be removed by iterative polishing, the initial maximum axis of inertia must be located to an accuracy of 3000 arcsec or a little less than a degree.

This can be achieved in an air bearing in spite of its potentially large torques which could cause an error between the true zero-g maximum axis and the apparent maximum axis. The adequacy of an air bearing is an experimental result, but it may be explained as follows: Since a symmetric rigid body executes polhodes with the apparent maximum axis of inertia at the center, it can be seen from Euler's rigid-body equations that a rotor-fixed moment, M , rotates the apparent maximum axis of inertia by an angle $\phi = M / \varepsilon_p h_G \omega_G$ radians where h_G is the angular momentum of the spinning rotor whose maximum axis is being measured. An estimate of the magnitude of M generated in an air bearing can be obtained by comparing it with the inertially-fixed moment which would cause typical drift rates, d , of 10 to 100 deg/hr for an air-bearing rotor spinning at 300 rad/sec. This is useful because the drift rates are much easier to see and hence are better known. Although the drift torques are inertially fixed and the maximum-axis error torques are rotor fixed, they can still be compared. This gives $\phi = d / \varepsilon_p \omega_G$ which shows the great lack of sensitivity of the maximum-axis error. For 10- to 100-deg/hr drifts, this expression gives about 0.1 to one deg between the apparent and zero-g axes, but this is much larger than the actual error since the mechanisms by which an air bearing generates rotor-fixed moments is very weak. Thus the robustness of the principal-axis direction combined with the relatively small magnitude of the rotor-fixed air torques makes an air bearing acceptable for the initial flat placement.

In a high-quality bearing, the offset of the rotor center of mass perpendicular to a vertical spin axis becomes the more severe effect. The size of this offset

can be estimated from the lack of roundness of the sphere. If $\varepsilon_{err} \approx 10^{-6}$ is the effective fractional polishing error of the initial rotor which will be assumed to also give the offset when multiplied by the rotor radius, the apparent maximum-axis error from gravity acting on the offset is given by $5 g \varepsilon_{err} / \varepsilon_p a \omega_G^2$. For $\varepsilon_p = 10^{-4}$, this is about 50 arcsec in an air bearing with $\omega_G \approx 300$ rad/sec and about 0.12 arcsec in an electric bearing with $\omega_G \approx 5800$ rad/sec. These considerations were borne out by the experience in the late 1960s although those rotors were commercial Beryllium-Copper spheres with an ε_{err} of about 10^{-4} giving an offset of 5000 arcsec in an air bearing. In spite of this, it was possible to align the maximum axis to about one arcsecond at a given temperature and rotor speed with laser mass trimming [54], and to measure the zero-g maximum axis to about 4 arcsec [55]. (In an isotropic material there is no sensitivity of the principle-axis direction to temperature in the zero-g conditions of space. It is only important in an earth-bound laboratory due to the temperature variation of the center of mass relative to the effective center of support.)

Thus to locate the initial maximum axis of inertia of a newly polished sphere, the rotor is placed in an air bearing with eddy-current torquing coils and/or a pair of jets to provide the spin motor. The rotor can be damped by rubbing it with a small soft brush or the polhodes can be traced out by putting successive ink dots at the spin axis. This generates a marked rotor which looks like the one in the frontispiece of Deimel's book [56] and locates the maximum axis to an accuracy of a few degrees. Next a grid (which will be covered up when the flat is polished on the rotor) is inscribed over this spot, the rotor is cleansed, and a short perpendicular synchronizing line is drawn on the equator to optically trigger a signal synchronous with rotor spin. The rotor is then placed in an air bearing which also has three pairs of orthogonal eddy-current torquing coils that can apply a moment perpendicular to the spin axis, and the rotor is doubly illuminated with white DC light from an ordinary incandescent lamp and with a stroboscope which is synchronized to the spin speed. When the rotor surface is observed under a microscope, the spin axis can be seen as a set of concentric circles of the white DC light reflecting off of tiny surface imperfections; and the polhoding causes the surface as seen in the strobe light to move under the microscope crosshairs centered on the concentric circles much like a city in the sights of a bombardier in an old WW II movie. The maximum axis is to the left of the motion; and by hooking the torquing coils to a joy stick so that it generates rotor-fixed torques proportional to its displacement, a visually steered active damper can be constructed which will drive the spin axis to the maximum axis of inertia [53]. Using this technique, the location of the apparent maxi-

mum axis on the inscribed grid can be found to a few arcseconds.

Next two optical flats are polished on the rotor, and it is placed in an electric bearing mounted on a three-axis table with an autocollimator at each end. The error in the flat placement is then determined [54, 55], and the flats iteratively polished to eliminate the error. If necessary, the difference between the apparent and zero- g maximum axes can be determined by plotting the flat error as a function of spin speed; but as seen above, the error in the electric bearing is only about 0.12 arcsec. In addition the spin axis can be rotated to be either vertical or horizontal, and the electric body-fixed moment determined. The anticipated improvement in accuracy over the results of the 1960s comes about by improved rotor polishing (now routinely done to about one μin , i.e. about a part in 10^6 [28]), by the use of an electric bearing with the correspondingly higher rotor spin speeds and well defined disturbing torques, and the three-axis table which eliminates the need for a torque motor during the measurements and which allows the spin axis to have any orientation between horizontal and vertical. Using these techniques, the zero- g axis can be measured to better than one mas and the flats can be aligned with this axis to at least 0.1 or 0.2 arcseconds.

Appendix E. Telescope Performance

Appendix E1 Telescope Noise Equivalent Angle

The telescope noise equivalent angles are calculated using the method of spectral integration, i.e. by integrating the product of the star, photodetector, and filter spectral responses rather than the monochromatic approximation which uses the peak wavelength of the star. It is better to integrate over the spectral responses since the monochromatic approximation underestimates the photon noise by about two thirds. The method of spectral integration and the formulas for the noise equivalent angles are derived in [43].

Although the photon beam is divided among multiple detectors, it is convenient to express the noise angle in terms of the total number of photons detected by all detectors. The number of photons detected depends on the quantum efficiency, $\eta(\lambda)$, of the detector which is just the responsivity scaled by $hc/\lambda e$ so that

$$\begin{aligned} \eta(\lambda) &= \frac{hc}{\lambda e} R(\lambda) = \frac{1.2398 \times 10^{-6}}{\lambda} \frac{\text{watt-m}}{\text{Amp}} R(\lambda) \\ &= 2.2543 \frac{\lambda_0}{\lambda} R(\lambda) \frac{\text{watts}}{\text{Amp}} \end{aligned} \quad \text{E1}$$

where $R(\lambda)$ is the detector responsivity in Amps/watt, e is the electronic charge, and $\lambda_0 = 5500 \text{ \AA}$. Since a star's visual magnitude is defined by a photon flux, S , at 5500 \AA such that $S(5500 \text{ \AA}) = 10^{-m_v/2.5} \times 1.053 \times 10^7$ photons/sec/m²/A^o; the total number of photons/second detected by all detectors, n , is given by

$$n = A_T 10^{-m_v/2.5} S_{nqe} \int_0^\infty R(\lambda) W(\lambda) \left(\frac{\lambda_0}{\lambda} \right)^5 \left[\frac{e^{x_0} - 1}{e^x - 1} \right] d\lambda \quad \text{E2}$$

where $S_{nqe} = 1.053 \times 10^7$ photons/sec/m²/A^o \times 2.2543 watts/Amp = 2.373×10^7 watt-photons/sec/m²/A^o/Amp, $W(\lambda)$ is the IR window transmission function, and A_T is the effective area of the telescope primary calculated below. $x = hc/\lambda kT$ and $x_0 = hc/\lambda_0 kT$ where T is the temperature of star so that the incident flux has been scaled to match the visual magnitude of the star at 5500 \AA . Using Equation E2, the noise equivalent angle of a single axis is given by

$$\theta_n =$$

$$\frac{1.22 \pi \sqrt{n}}{2 A_T D_T 10^{-m_v/2.5} S_{nqe} \int_0^\infty \frac{R(\lambda) W(\lambda)}{\lambda} \left(\frac{\lambda_0}{\lambda} \right)^5 \left[\frac{e^{x_0} - 1}{e^x - 1} \right] d\lambda} \quad \text{E3}$$

Table E1 shows the results of the noise calculations for the most likely candidates for the reference star. The number of detected photons per second, the detected-photon noise equivalent angles, and the detector-dark-current noise equivalent angles at room temperature are shown for two detectors; a Burle Industries Gallium Arsenide C31034A photomultiplier and a Hamamatsu R4632 photomultiplier. The C31034A which is a Gallium Arsenide device has especially high ambient-temperature dark current. For this reason it is typically operated at -30°C , but the number of detected photons in this application is so large that the ambient-temperature dark noise of the C31034A is acceptable. The effective primary area is determined as follows: counting the Schmidt corrector, the primary and secondary mirrors, four tipping plates, the pyramid prism, the refocusing reflectors, and the refocusing lenses; there is the IR window with a transmission of 0.75 (assuming $W(\lambda) = 1$), four reflecting surfaces with a transmission of $(0.97)^4$, six bulk absorptions with a transmission of $(0.9995)^6$, and twelve refractive coatings with a transmission of $(0.985)^{12}$ making a total transmis-

sion in the optics of 0.552. Counting a central obscuration with a diameter of 10 cm, the total telescope

transmission becomes 0.518 giving an effective area of 0.065 m² down from 0.126 m².

Name	Declination (deg)	Det Ph/sec Burle Ga As C31034A	Det Ph Noise $\mu\text{as}/\text{Hz}^{1/2}$	Dark Noise $\mu\text{as}/\text{Hz}^{1/2}$	Det Ph/sec Hamamatsu R4632 PM	Det Ph Noise $\mu\text{as}/\text{Hz}^{1/2}$	Dark Noise $\mu\text{as}/\text{Hz}^{1/2}$
Achernar	-57.24	1.01E+09	7.7	1.8	9.80E+08	6.5	0.021
Rigel	-8.202	9.34E+08	9.1	3.2	7.40E+08	8.8	0.032
Capella	46.00	6.34E+08	15	10.6	3.08E+08	19	0.106
Mintaka	-0.2992	2.56E+08	14	6.4	2.91E+08	11	0.064
Nair al Saif	-5.917	1.58E+08	18	10.3	1.81E+08	14	0.103
Alnilam	-1.202	3.86E+08	12	4.6	4.19E+08	9	0.046
Canopus	-52.70	1.48E+09	8.5	3.0	9.45E+08	9.2	0.030
Sirius	-16.72	3.43E+09	5.1	1.0	2.48E+09	5.2	0.010
Procyon	5.225	5.02E+08	16	10.2	2.93E+08	18	0.102
Mimosa	-59.69	5.79E+08	9.6	3.0	6.35E+08	7.6	0.030
Hadar	-60.37	1.01E+09	7.4	1.8	1.07E+09	5.9	0.018
Arcturus	19.18	7.23E+08	15	10.8	3.13E+08	19	0.108
Rigel Kent	-60.84	6.98E+08	14	8.2	3.79E+08	16	0.082
Vega	38.78	8.90E+08	9.9	3.9	6.53E+08	10	0.039

Table E1. Detected-Photon Noise for Selected Bright Stars and a 40-cm Telescope.

The stars in Table E1 generally have acceptable noise performance with both types of photomultiplier, but they naturally fall into certain groups which are useful for different mission emphases. The low declination stars: Mintaka, Nair al Saif, Alnilam, Procyon, and Rigel give the best drift performance; and Mintaka or Alnilam would be best for a four-satellite mission doing a simultaneous high-precision geodetic and frame-dragging experiment using only one star. This is because their very small declinations guarantee that the declination-time condition, the product of declination and experiment time must be less than $8 (r_s / R_e)^2 / 3 J_2 n$ in a polar orbit, *e.g.* 450 arcmin-years at 1500 km [27, 2], is fulfilled for long missions which in turn guarantees that the gravity-gradient-drift angle will also return to zero in the frame-dragging case. The hot, distant, O and B stars: Alnilam, Mintaka, and Rigel have the least inherent proper motion uncertainty. The very hot O and B stars: Mimosa, Nair al Saif, Mintaka, and Alnilam would have better noise performance if acceptable UV optics and photomultipliers could be found. The very close stars: Rigel Kent, Sirius, and Procyon would give the best chance of seeing earth-like planets (Cf. Appendix H5), but the intermediate-distance stars: Achernar, Capella, Arcturus, and Vega might also reveal small planets. The medium-temperature main-sequence stars: Sirius,

Vega, and Rigel Kent would be of the most interest if earth-like planets were detected around them.

Appendix E2. Telescope Zero-Point Errors

As with the autocollimator, the telescope zero-point errors are eliminated by spinning the satellite (Cf. Section 5 and Appendix F). Since the telescope looks at inertial space, however, any change in the effective center of the incoming light is fixed in inertial space and is not removed by spinning the satellite. In addition to proper motion, subtraction of the results of two experiments looking at the same star also suppresses these errors. They include any change in the background light of the very faint distant stars and galaxies (a remote supernova or quasar flare), varying background nebulosity, any change in the centroid of the star's light, polarization of the starlight, gravitational bending of the incoming light by the sun, etc. Some stars have a detectable polarization in their light, and this would be seen in the telescope via transmission through the tipping plates. This error is theoretically zero since it is at twice roll frequency, but a subharmonic component could be generated by tipping plate oscillations for example. In any event all common-

mode problems are eliminated to the accuracy of the instruments by subtraction.

Although like the autocollimator the zero-point offset drift is removed by the satellite spin, it is still useful to know its size. The absolute offset drift of the telescope is determined principally by the thermal temperature coefficient of the materials and is of the order of 5×10^{-7} rad/K/meter = 100 mas/K/meter. The electronic offset with FET or JFET operational amplifiers is much smaller, of the order of $0.05 \mu\text{as/K}$. With absolute temperature control to 0.1 K and a typical telescope size of one meter, the absolute zero point drift is expected to be less than 10 mas.

Appendix E3. Telescope Scale-Factor Errors

In order to keep the telescope scale-factor errors in bound it is necessary to operate the telescope as close to null as possible. For an accuracy of $0.2 \mu\text{as}$ and a limit on the linear range of 10^6 , the apparent angle between the gyro spin axis and the star cannot exceed 0.2 arcsec. This is accomplished by using the orbital aberration of starlight to cancel the relativity drift. Since the annual aberration of starlight can be as large as 40 arcsec, high precision measurements in null can only be made at the beginning and end of the experiment, one year apart, when the annual aberration returns to its starting value. Using the telescope coarse tipping plates, measurements could be made and averaged over the whole year; but high-precision data would only be taken at the beginning and the end.

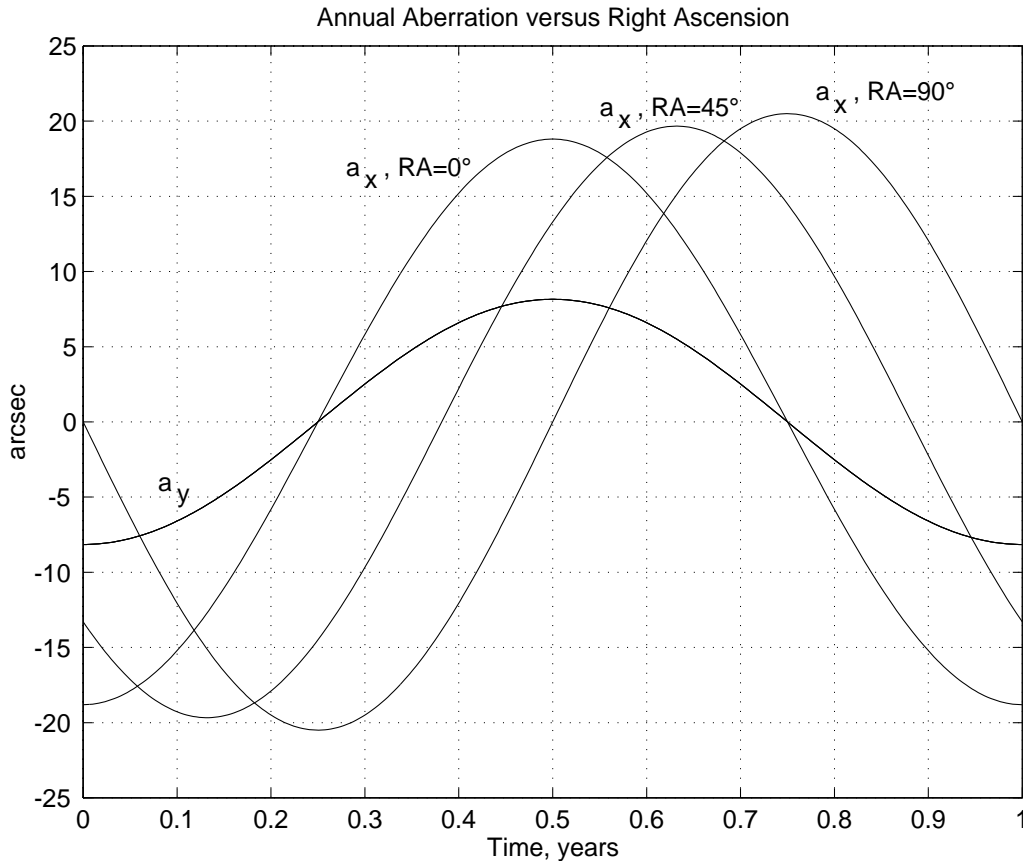


Figure E1. Annual Aberration Signals for Various Star Right Ascensions

With this strategy, the important question becomes how long does a ± 0.2 arcsec null last, i.e. how much averaging time is available for the telescope and autocollimator noise equivalent angles? In the star coordinate system with the z -axis toward the star, the x -axis making the smallest angle with north, and ω_a

equal to the earth's mean annual orbital rate; the non-spinning x - and y -telescope annual aberration angles are given by

$$a_{xa} = -\sin^{-1}\left(\frac{v_{mo}}{c}\right) [\sin \omega_a t \sin \alpha + \cos \omega_a t \cos \alpha \epsilon] \quad E4$$

and

$$a_{ya} = -\sin^{-1}\left(\frac{v_{mo}}{c}\right) \left[s\omega_a t s\delta c\alpha + c\omega_a t (c\delta s\epsilon - s\delta s\alpha c\epsilon) \right]$$

E5

where α and δ are the star's right ascension and declination, ϵ is the obliquity of the ecliptic, and v_{mo} is the velocity of the earth in its orbit which is assumed to be circular. Figure E1 shows plots of a_{xa} and a_{ya} for a declination of zero degrees and three right ascensions, 0, 45, and 90 degrees. It can be seen that each aberration curve has a maximum or a minimum twice per year when the aberration changes only slowly, and the aberration angle remains within ± 0.2 arcsec for about 23 days for x and about 36 days for y . For small declinations and stars close to the equinoxes, the x - and y -curves are almost in phase, and it possible to remain within ± 0.2 arcsec for 23 days in both axes. For stars with right ascensions other than zero or 180 deg, the x -aberration angle dephases from the y -angle, drastically reducing the time that both axes are in null. In the extreme case of 90 deg, the time in null is only two or three days for some stars giving a very small averaging time. There is a way around this problem, however, such that the maximum null time of 23 days may be had for a star with any right ascension. To see this, the exact method of cancellation of the relativity drift by the orbital aberration must first be considered.

It can be seen from Table 1 that orbital aberration can be used to exactly cancel the relativity drift at any altitude above 1560 km and to cancel it with a maximum error of 0.8 arcsec at altitudes above 1000 km. To effect this cancellation the measurements are made in different parts of the orbit at the start and end of the experiment. The gyro alignment is initialized when the satellite is over the ± 90 -deg points with respect to the star where the orbital aberration is zero, i.e. the angle measurement between the star and the gyroscope is averaged during the approximately 90 seconds at each 90-deg point while the aberration is within the 0.2 arcsec null. This is repeated for as many orbits as possible until the change in the annual aberration makes it no longer possible to come into null. At the end of the year the angle between the gyro and the star is read when the orbital aberration is close to the maximum, i.e. when the satellite is close to the equator defined by the star (zero-degree point). Since orbital aberration and the geodetic relativity drift are in the same direction, they then cancel one another. Again the number of orbits where data can be taken is limited by the change in the annual aberration. In order to get around the difficulty of dephasing and have the maximum time that the annual aberration is within ± 0.2 arcsec, the experiment is initialized at one of the two

times per year when the x -aberration angle is at a maximum or a minimum giving the full 23 days in that axis. In the case of the y -axis, the aberration angle is rapidly changing and the null is much shorter than 23 days for stars that do not lie close to the equinoxes. The y -axis, however, is the experiment axis; and the annual-aberration y -angle can be canceled at each pass with the orbital aberration by moving the point at which data is taken a little bit before or after the exact position at the ± 90 -deg points or at the zero-degree point. In this way any star can have the full 23 days of null. For the first in the series of one-year experiments where the relativity geodetic drift and the orbital aberration are almost equal, this option is not available at the end of the experiment at the zero-degree point; but this is not a serious drawback since the time in the orbital null is about five times as long at the zero-degree point, 900 seconds compared to 180 seconds. As the series of one-year experiments progresses and the altitude is raised in 100-km increments, more and more freedom becomes available at the zero-degree point to advance or retard the measurement to cancel the annual aberration.

Thus 23 days are available at the ± 90 -deg points with about 12.4 orbits per day and 90 seconds at each point, and this gives a total averaging time of about 26,000 seconds counting the fact that the total must be reduced by about half because the full ± 0.2 arcsec is not available at the edges of the cancellation. At the zero-deg point, this time is five times larger, 130,000 sec. In the case of the autocollimator, the times are further cut in half by the chopping. If the noise equivalent angle of the telescope is $10 \mu\text{as}/\text{Hz}^{1/2}$, the error after 26,000 seconds of averaging is approximately $0.05 \mu\text{as}$. Having sufficient averaging time to always be able to make the telescope measurements within a range of ± 0.2 arcsec lessens the severity of the scale-factor problem by a factor of 100 to 200 over an experiment which averages over the entire year.

There is an additional advantage to setting the start and end times at the maximum or minimum values of the x -aberration. These occur when the earth, sun, and projection of the star into the plane of the ecliptic all lie in a straight line. When the order is sun-earth-star, the sun shines on the back side of the spacecraft so that the telescopes are in the vehicle's shadow when the precision data is taken; and the satellite itself is mostly on the night side of the earth. The angle between the sun and the $-z$ -axis of the vehicle is equal to the ecliptic latitude of the star. Table E2 shows the start/end date and the ecliptic and galactic latitudes of selected bright stars. It can be seen that in most cases, the sun is almost directly behind the spacecraft because the ecliptic latitude is small. The galactic latitude has no relevance to the sun angle, but it is also shown because it gives an idea of the density of faint background stars.

Star	RA (deg)	Declination (deg)	Start/End Date	Ecl Lat/ Sun Angle	Gal Lat
Achernar	24.425	-57.25	19-Oct	-59.4	-58.7
Rigel	78.643	-8.202	11-Dec	-31.1	-25.0
Capella	79.171	46.00	12-Dec	22.9	4.73
Mintaka	83.001	-0.2992	15-Dec	-23.6	-17.5
Nair al Saif	83.858	-5.917	16-Dec	-27.4	-18.5
Alnilam	84.053	-1.202	16-Dec	-24.5	-17.0
Canopus	95.988	-52.68	27-Dec	-75.8	-25.1
Sirius	101.29	-16.72	1-Jan	-39.6	-8.65
Procyon	114.83	5.233	28-Jan	-16.0	13.3
Mimosa	191.93	-59.70	2-Apr	-48.6	3.17
Hadar	210.96	-60.37	23-Apr	-44.1	1.21
Arcturus	213.92	19.18	26-Apr	30.7	68.9
Rigel Kent	219.90	-60.83	2-May	-42.6	-0.738
Vega	279.23	38.78	30-Jun	61.7	19.0

Table E2. Start Date and Sun Angle of the Bright Stars

The question now arises how to design the telescope to cover the linear range from zero to 0.2 arcsec with a scale-factor error of the order of 10^{-6} . This can be done by reading out the rotation angle of two servo-controlled tipping plates which center the diffraction spot on the pyramid prism. If the telescope has a focal length of 10 meters, the movement of the image spot at maximum deviation of ± 0.2 arcsec is ± 10 microns. For small angles, the lateral displacement of the beam caused by a tipping-plate rotation, θ , is given by $\theta t(n-1)/n$ where t is the thickness of the plate and n is its index of refraction. For $n = 1.5$, a 150-micron thick tipping plate can zero a deviation of ± 10 microns with a maximum rotation of approximately ± 10 degrees. In order to avoid the problem of converting an analog signal with an accuracy of 10^{-6} or better which would require an AD converter with at least 20-bit accuracy, the tipping plate is rigidly connected to an 11-bit angle encoder with 2048 divisions per 20 degrees at the 11th bit. The last bit is divided by an analog signal which is obtained from a capacitive coupler also consisting of 2048 plates per 20 degrees (18432 in the full circle) on the outer radius of the encoder. This analog signal is converted with a 12-bit AD converter giving a total of 23 bits ≈ 8.4 million without requiring a 23-bit AD converter. This corresponds to a resolution of approximately $0.05 \mu\text{as}$ in reading $\pm 200,000 \mu\text{as}$. In addition to the analog signal from the last bit division, the tipping-

plate servo mechanism makes errors of the order of $30 \mu\text{as}$ in centering the diffraction spot on the prism. Because of this, it is necessary to correct the analog measurement with the raw light signal to get the last one or two orders of magnitude of accuracy.

The accuracy with which the $8.14\text{-}\mu$ wide plates can be laid down on the angle encoder is about 0.1μ which corresponds to an error of about 0.2 arcsec at a radius of 10 cm. Although full scale corresponds to ± 10 degrees for the tipping plates, the entire circle of the angle encoder would be used for the capacitive divider. With 18432 plates, the $0.1\text{-}\mu$ error would be reduced by a further factor of about $(18432)^{1/2} \approx 136$ by smoothing, so that the final angle-encoder error would be of the order of 2 mas. Since the amplification of the tipping plate is $nf/t(n-1) = 2 \times 10^5$, an angle-encoder error of 2 mas corresponds to a readout error of $0.01 \mu\text{as}$. Because of these considerations and the symmetry properties of a full circle, only very minimal calibration of the angle encoder is required. The cross-axis bearing stability requirements are similar. Assuming a 10-cm axis, a bearing-centering stability of about 0.1μ or $4 \mu\text{in}$ translates into an angle-encoder error of 0.2 arcsec which in turn corresponds to a readout error of one μas . This would also be reduced by about one or two orders of magnitude by the averaging of the bearing noise.

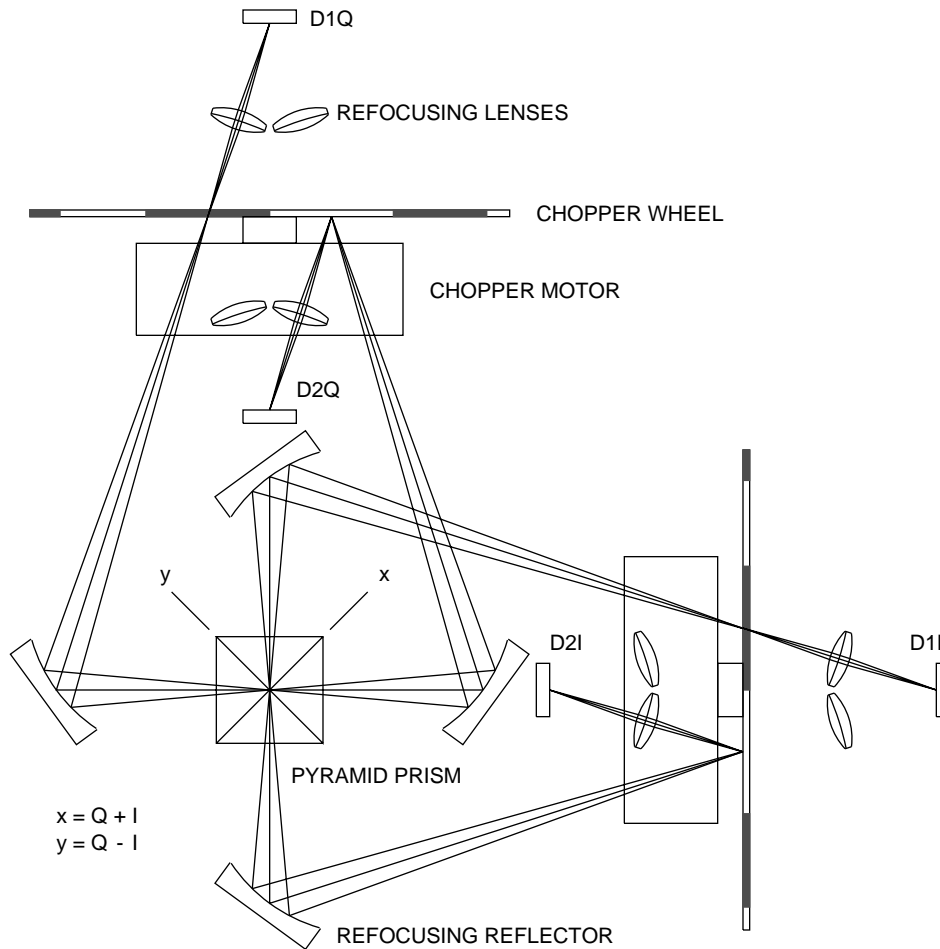


Figure E2. Telescope Readout Light Path

The photodetectors for the telescope have the same stability problem as with the autocollimator, and in the case of the telescope there is no calibrating signal to hold the gain stable. The problem can be solved, however, by chopping which also eliminates the $1/f$ noise. Figure E2 shows the detector arrangement and the light path after the prime focus at the tip of the pyramid prism¹⁰. In the figure the focused light from

the telescope arrives at the point of the prism downwards along a line perpendicular to the page. The tipping plates (not shown) are just above the pyramid prism. The diffraction spot is focused onto the point of the pyramid prism for maximum sensitivity and then the pairs of split beams are refocused on the detector D1 by the concave reflectors and the refoocusing lenses. A fan-blade chopper wheel exactly cuts off one of the two beams, and the interrupted beam is reflected to detector D2. Thus D1 and D2 alternately see the plus and minus beams, and the servo error signal is always generated from the same detector. Detector scale-factor drift then plays an insignificant role since the tipping-plate servo holds the two beams in close balance.

¹⁰ A beam splitter and two roof prisms [53] could be used to process the image instead of the pyramid prism, but this has the additional complication of a possible curvature of the roof prism edge. If the roof prisms were to be used, the light path from a single roof prism would be the same as one half of Figure E2 with only one chopper and one set of reflectors and detectors. A system with two roof prisms has the advantage that the prisms are perhaps easier to manufacturer, and the tipping

plates would be single-axis devices. The noise for the roof prisms is $2^{1/2}$ greater than for the pyramid prism, and the noise values in Table E1 are for a pyramid prism with only one detector or roof prisms with detectors D1 and D2.

The chopper shaft frequency is about 0.5 Hz which combined with a 10-blade wheel gives a chopping frequency of 5 Hz. The very low shaft frequency combined with precision bearings and precision wheel balancing eliminates vibration as a problem. The chopper has many other sources of error, but the system can be designed so that they do not effect detector D1 because its beam passes the chopper unimpeded. This is done by blocking the measurement when the beam is switched so that switch-over errors due to blade imperfections and the finite beam width are eliminated. In addition to vibration, the chopper errors are: unequal angular size of the openings, misalignment of the wheel plane with respect to the chopper shaft, misalignment of the shaft bearings with respect to the optical axis, bearing noise, desynchronization of the wheel angle with respect to the demodulation signal, and wheel flatness errors. These errors mostly affect D2 but not D1 because they affect the centering and the focus of the light which falls on D2 since it is reflected from the wheel surface, and they could potentially require that the data from D2 not be used.

In addition to scale-factor errors caused by the readout, coma in the telescope also generates a scale-factor error. The Schmidt telescope can be designed to

reduce coma to about $100 \mu\text{as}/\text{arcsec-off-axis}$, and the rest can be removed by calibration. Because the telescope signal is chopped, the absolute stability of the scale factor is determined principally by the thermal expansion coefficients of the materials and is about $5 \times 10^{-7} / \text{K}$ for a truss made of Invar.

Appendix F. Roll-Coupled Zero-Point Errors and Drifts

Since satellite spin is used to separate the zero-point errors and drifts from the science data, any contribution to an instrument zero point which had a component at the satellite roll frequency would cause a measurement error. If the amplitude of any such term drifted over the course of the year while the experiment was in progress, it would constitute an error in the experimental result. For this reason the gyro and the instruments, telescope and autocollimator, are surrounded by a thermally insulated, mechanically and electrically isolated enclosure. The instrument zeros shift because of mechanical deformation and because of change in the electrical balance of the photodetectors and their operational amplifiers. Table F1 shows a summary of the results of the calculations of the roll-coupled zero-point errors.

	Roll-Coupled Zero-Point Errors	Summary: (μas)
Thermal Leakage	Thermal deformation of the truss structure Thermal deformation of the telescope Thermal deformation of the autocollimator	5.7E-04 5.7E-04 5.7E-05
Mechanical Leakage	Transmitted satellite thermal deformation Thruster-caused mechanical deformation Tipping-Plate-caused mechanical deformation Subharmonic tidal deformation	0.01 4.5E-06 5.0E-13 4.1E-07
Elec. Leakage	Power supply roll frequency ripple, see text.	0
Telescope Electronic Offset	Telescope photomultiplier unbalance Telescope op amp, input offset current Telescope op amp, input offset voltage	1.1E-08 5.5E-07 5.5E-10
Autocollimator Electronic Offset	Autocollimator photodetector unbalance Autocollimator op amp, input offset current Autocollimator op amp, input offset voltage	5.5E-08 5.5E-10 5.5E-10
	Zero-Point Error RSS	0.010

Table F1. Roll-Coupled Zero-Point Errors

The first group of errors is the distortion of the telescope and autocollimator frames and of the truss structure which supports the instruments caused by temperature gradients inside of the enclosure which oscillate at roll frequency. The deformation of the truss can cause an error angle between the telescopes and the autocollimators, and a deformation of an autocollimator or a telescope causes a direct mechanical shift of its zero point. If the heights and widths of the instruments are roughly equal, then the angle error is simply the temperature coefficient of expansion of the material times the temperature difference. The thermal expansion coefficient used was that of Invar, $5 \times 10^{-7} / \text{K}$. In addition to Invar, Zerodur glass with a thermal coefficient of expansion of $5 \times 10^{-7} / \text{K}$ can be used for the telescope optics; and in difficult situations, Superinvar with $1 \times 10^{-7} / \text{K}$ is available.

The second group consists of the errors caused by mechanical deformation in the satellite which couples to the truss structure inside of the enclosure which mounts the telescopes and the gyro assembly including the autocollimators and magnetic shield. The largest error in this group comes from the thermal distortions of the satellite structure outside of the enclosure which are transmitted mechanically to the truss structure on the inside. To keep this error within bounds the support of the structure must be carefully designed. At this time for the purpose of calculating the size of this effect, it will be assumed that the truss structure is coupled to the rest of the satellite at a single point. Once in space this is not a problem; but to survive launch, other support points are required. It is assumed that these additional

support points are severed just after orbit insertion. The satellite distortion angle is assumed to be given by the thermal coefficient of expansion of Aluminum, $2.5 \times 10^{-5} / \text{K}$, times the assumed roll-frequency amplitude of the temperature of the satellite structure, 0.1 K. Although the outside skin temperature variation would be about 10 K, the structure is temperature controlled to about 0.1 K in roll. The transmission of the structural deformation to the inner truss was calculated by a finite-element model and was found to be about $0.01 \mu\text{as}$ [57].

The balance of the errors are very small, but they are included for completeness. The thruster deformation assumes that the truss is deformed by the force from the drag-free thrusters which would have a component at roll. The magnitude of the thruster forces was taken from the drag at a solar maximum or the solar radiation pressure which are about the same magnitude. The tipping-plate error comes from the fact that it must oscillate at roll frequency and the reaction torque distorts the truss. The tidal distortion is theoretically zero since it occurs at twice roll frequency, but there might be some conceivable mechanism where the oscillations did not return to exactly the same point causing a subharmonic term. The amplitude in the table was calculated by multiplying the amplitude of the tidal distortion by 0.001 as an estimate of the subharmonic amplitude. The amplitude of the electronic offsets were calculated in the standard way by multiplying the temperature sensitivities of the offset voltages and currents by the roll temperature amplitude and translating this into the equivalent angle.

Temperature and Temperature Gradient in Roll	K or K/meter
Temperature waves through the insulated enclosure walls	3.84E-09
Temperature waves through 33 cm of copper power leads	3.99E-09
Roll-temperature amplitude at the telescope IR window	1.00E-11
Roll-temperature amplitude at the vacuum exhaust port	1.00E-12
Roll-temperature due to roll ripples on the power bus	2.49E-10
1100th orbital harmonics	3.47E-12
RSS Roll-Temperature Amplitude	5.54E-09

Table F2. Temperature and Temperature-Gradient Amplitudes at Roll Frequency

Finally the roll-frequency variations of temperature and temperature gradient inside of the thermal enclosure must be calculated. Table F2 shows the results of this calculation. Temperature influences from roll-coupled heating of the spacecraft by the sun and the earth's IR can enter the enclosure as temperature waves

through its insulated walls, along the copper in the power and communication cables, through the telescope aperture, through the vacuum exhaust ports, and by internal heating caused by ripples on the power bus. In addition, approximately the 1108th harmonic of the orbit frequency lies at the roll frequency. Using a square-wave model there is a small outside temperature varia-

tion equal to approximately the orbital variation in spacecraft skin temperature divided by 1100. This is a very tiny effect; but the question occasionally comes up, so it is included here.

The calculations shown in the table only give the roll temperature amplitude at the output of the leak-

age source and do not take into account the heat capacity of structures or temperature waves inside of the enclosure. These would have the effect of further attenuating the temperature amplitudes. No distinction is made in the calculations between temperature and temperature gradient since the size of the satellite is of the order of one meter.

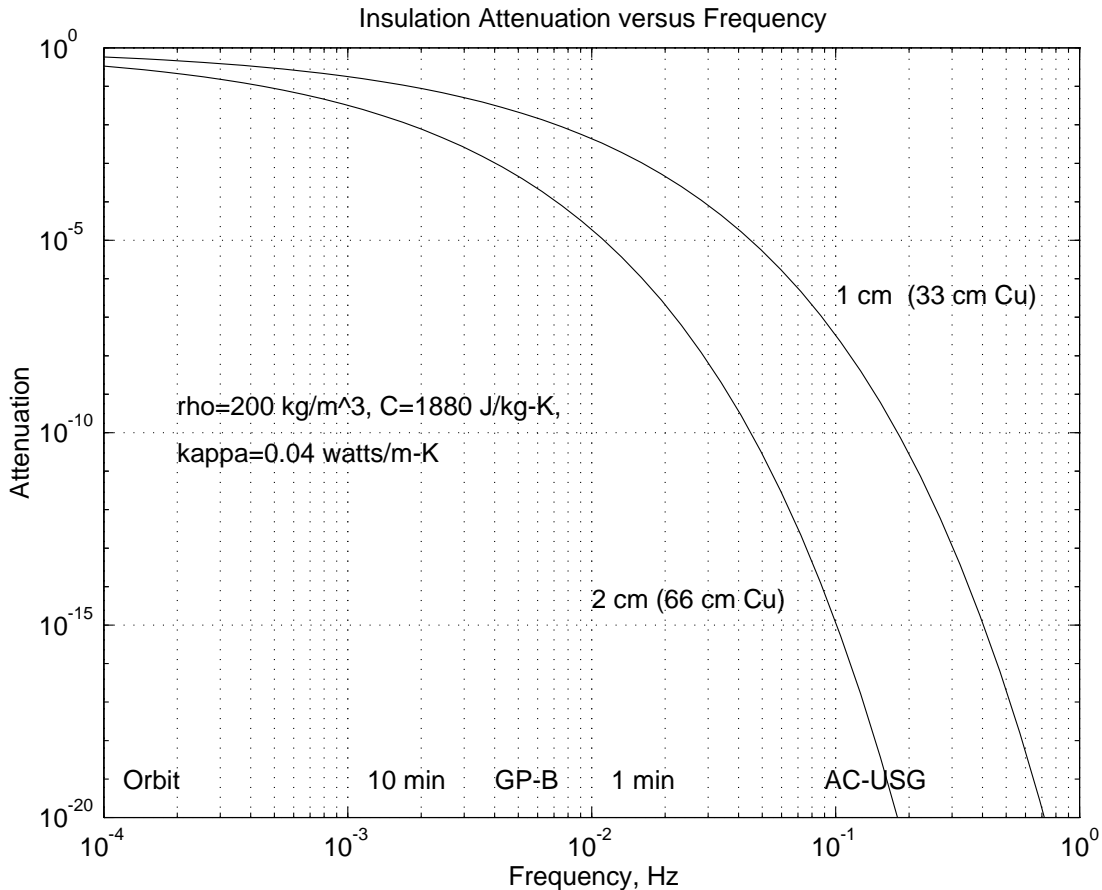


Figure F1. Temperature Wave Attenuation versus Satellite Roll Frequency, $\omega_s / 2 \pi$

The most important roll-temperature source is temperature waves through the insulated walls. The calculation of this effect is done in the classical manner using the result of wave attenuation calculated from a sinusoidal input to the diffusion equation. The characteristic length is given by $L = (2\kappa / C\rho\omega_s)^{1/2}$ where κ is the thermal conductivity of the insulation, C its specific heat capacity, and ρ its density. The roll-temperature amplitude is then given by the outside temperature amplitude times $\exp(-t_w/L)$ where t_w is the thickness of the insulation and the outside temperature variation is assumed to be 10 K. In this calculation t_w was taken as one cm, and for typical insulation, κ as 0.04 watts/m/K, ρ as 200 kg/m^3 , and C as 1880 J/kg/K resulting in a

characteristic length of 0.46 mm. An interesting point is that the characteristic length for copper is 15 mm, i.e. only about 33 times as long although the conductivity differs by orders of magnitude. This means that a power cable of length 33 cm has the same attenuation as an insulating wall one cm thick and allows temperature variations from this source to be suppressed. The other interesting thing about this calculation is that because of the exponential, a loglog plot of the attenuation versus frequency is not a straight line but an ever steepening curve in the downward direction. This means that beyond a certain roll frequency, roll temperature variations essentially vanish; and conversely, too slow a roll frequency does not achieve very much.

This is shown in Figure F1. For this reason the satellite roll frequency has been chosen at one rad/sec, and it is basically this high roll rate which eliminates many of the problems from roll-coupled errors.

The telescopes are completely enclosed in the thermal enclosure and look into space through an IR window which is designed to prevent heat leaking out of the enclosure and to attenuate roll temperature variations entering the cavity. Outside of the enclosure, the telescope field of view is protected from sunlight and earth albedo and IR by a cylindrical shield one or two meters long with about ten equally-spaced flat ring-shaped baffles inside. These shields were developed for earth-observing satellites and are available as off-the-shelf items. They are stowed for launch in collapsed form like a stove-pipe hat and are deployed in orbit with an internal spring. They can also have a shutter at the end which can be closed if needed, for example, at the six-months point when the sun can shine almost directly into the telescope as shown in Table E2. The roll-temperature amplitude at the telescope window is calculated by assuming an IR window attenuation of 0.01 and an attenuation of 0.1 per baffle. Roll-coupled IR radiation into the telescope from the sun shining into the end of the shield is then attenuated by 10^{11} . In addition to direct sunshine inside of the end of the shield, the sun could also heat the side of the shield at roll frequency. These sources are unlikely to be a problem during the precision measurements in null since, as explained in Appendix E3, the experiment can always be started and ended with the sun almost directly behind the spacecraft. For year-round measurements, they can be eliminated either by double shields or a reflective coating on the shield.

The power-bus ripples can be completely eliminated by having two batteries inside of thermal enclosures of their own which are alternately used while the other one is being charged from the power bus. Because of the extra batteries, it would be desirable not use this solution; but it provides a backup in case the power bus cannot be sufficiently regulated so it can be used directly. If the power-bus is used, the roll ripple amplitude must be held below approximately one microvolt.

Appendix G. Instrument Scale-Factor Calibration Accuracy

The coefficients of the calibration polynomials in Section 6 are determined by comparing known input angles with the telescope or autocollimator measurements. There are two instruments and only one calibration signal; but because the higher order terms are insignificant at small amplitudes, separate calibration of the autocollimator and telescope may be bootstrapped

by alternately controlling satellite attitude to the gyro and then to the telescope. Except for the measurement of the flat-misalignment error and satellite attitude control, however, separate calibration of the two instruments can be avoided by directly calibrating the difference angle between the telescope and the autocollimator.

Higher order unmodelled terms bias the modelled coefficients; and because of this at least a third order calibration polynomial must be used. The principal bias comes from the unmodelled odd powers of x (satellite spin eliminates the even-ordered terms), for example x^5 and higher if a third order model is used. Typical biases of the x -terms normalized to one can be calculated by multiplying the third-order least squares pseudoinverse matrix times the measurement matrix of a given term and are 0.1491 for x^5 , 0.1663 for x^7 , 0.1556 for x^9 , 0.1397 for x^{11} , etc. Unlike the covariance errors, the unmodelled bias terms do not decrease with increasing numbers of measurements; also the influences die out very slowly, for example x^{23} is 0.0729 and x^{39} is 0.0402. Slow convergence is not a problem, however, since the higher-order inputs decrease because the coefficients are washed out by the continuity of the tipping-plate polishing, the finite size of the beam, the continuity of the reticule lines, diffraction, optical aberration, etc. If only a first-order model had been used for the calibration, the unmodelled bias from just x^3 would have been 0.45 and would not have been sufficiently reduced by the above factors.

The question then arises as to the accuracy with which the calibration can be done, and this in turn depends principally on the total number of calibration points. Establishing the counter-rotating orbits requires about one year (Cf. Appendix H1), and the initial calibration can be done during this time. The gyro would be realigned every few days with a bright star and calibration measurements taken every satellite pass at the orbital point where the star is closest to the zenith with respect to the satellite. Around this point the orbital aberration remains within ± 0.2 -arcsec for about 900 seconds, and gyro drift and star proper motion are insignificant during 900 seconds. With approximately 12.4 passes per day, this gives a total calibration time of about 11000 seconds per day. Once an experiment run begins, each orbital measurement pass also includes 180 seconds of calibration check at the start of an experiment and 900 seconds at the end (Cf. Appendix E3). Also after the end of a one-year run, the calibration can again be checked in the same manner as prior to the run.

Figure G1 shows the calibration accuracy (RSS of the coefficient errors) versus the number of calibration points assuming an intrinsic stability of 10^{-7} and a one-second average for each point. The results in

Figure G1 are for a linear- and a third-order calibration polynomial in x and y . The curves marked "1st Order" and "3rd Order" are the RSS values of the errors in the calibration coefficients for each model, i.e. the square root of the trace of the covariance matrix. This gives the total error of the calibration coefficients, but it over emphasizes the errors of measurements made with this calibration. The reason is that not all of the measurements are made at full scale where the higher order terms would be important. If it is assumed that about one half of the measurements are made at one half of full scale or less, then a better approach is to weight the linear terms by 0.5 and the third-order terms by

$0.5^3 = 0.125$. This gives the curve that is labeled "Weighted 3rd Order" in the figure. The RSS of the linear terms in the third-order calibration are also shown for comparison in the curved labeled "3rd Order, Linear Only". Because the RSS of the trace of the covariance matrix increases as the order of the model increases, Figure G1 might give the impression that there is no cut off at higher orders; but this simply shows that increasing the order of the model increases the number of coefficients and hence their RSS value and emphasizes the fact that it is wrong to use a model with too many coefficients or to take the total RSS as a measure of system accuracy.

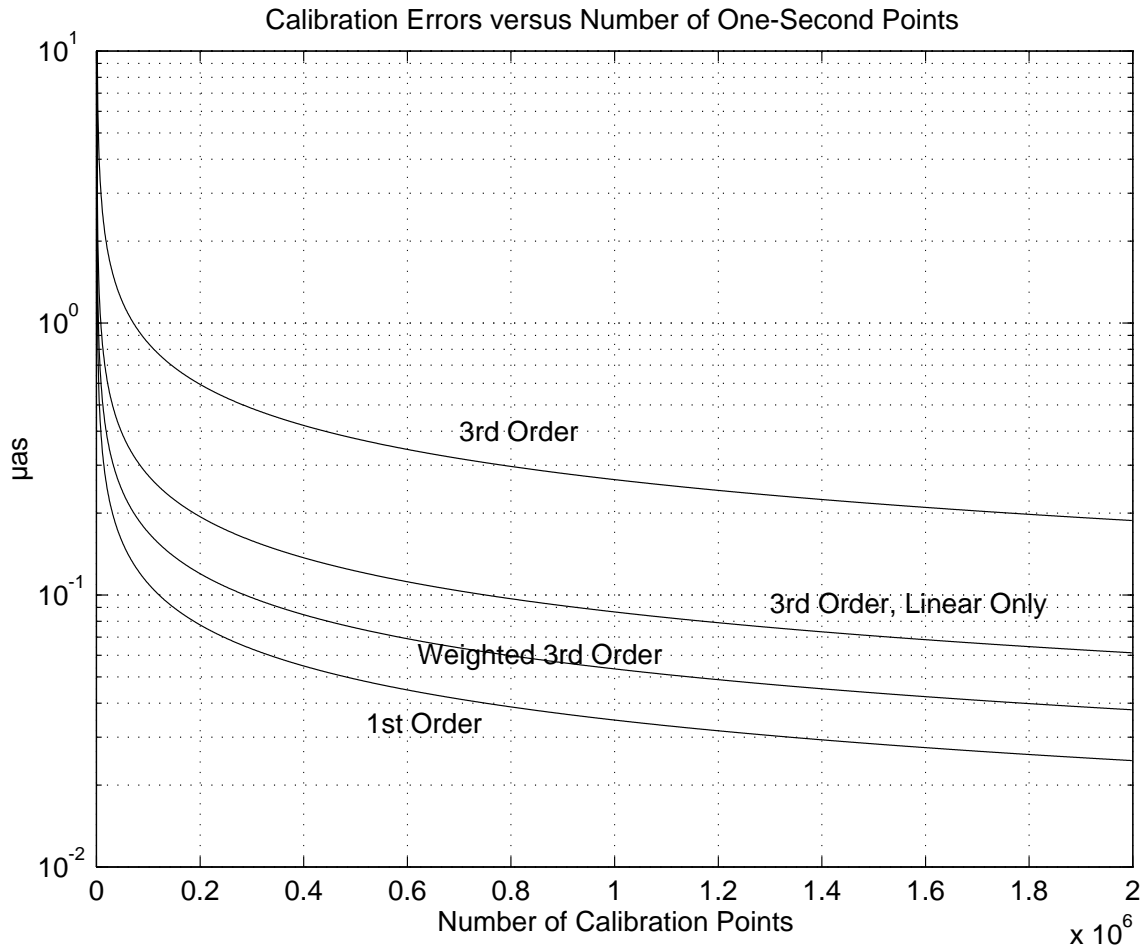


Figure G1. Scale-Factor Calibration Errors

The question now arises: How large are the scale-factor errors expect to be, and what are the errors due to the unmodelled terms? Because the use of a full circle greatly reduces calibration errors in the angle encoder, the principal errors will come from imperfections in the tipping plate. In addition to thickness variations,

the tipping plate has a beam displacement error due to a lack of parallelism, ϕ , given by $\phi t/n$ and an angle error for the outgoing beam of $\phi(n^2-1)/n$. These errors, however, are small compared to the errors caused by thickness variations. Assuming thickness errors of about 0.005μ ($0.2 \mu\text{in}$) which is about one hundredth of a

fringe, the resulting angle error for a $150\text{-}\mu$ thick tipping plate is about $7\text{ }\mu\text{as}$. For the n th-order terms, however, it will be assumed that this error is reduced by about n by the continuity of the polishing and by a further factor of n by the finite size of the beam which is slightly larger than full-scale displacement. Taking the RSS value of $7\text{ }\mu\text{as}$ times the fifth order and higher unmodelled biases listed in the second paragraph of this section divided by n^2 , the total error from the unmodelled terms is about $0.051\text{ }\mu\text{as}$. For the modeled errors, the weighted third-order curve, i.e. $0.04\text{ }\mu\text{as} \times 0.707 = 0.03\text{ }\mu\text{as}$, will be used as the system calibration accuracy. The factor of 0.707 arises because the odd symmetry means that each measurement gives two values, plus and minus; and because of this, the two million points shown in Figure G1 become four million. In calculating Figure G1, the discrete Kalman-filter covariance equation was solved with input noise arising from the stability model and measurement noise equal to a telescope noise density of $10\text{ }\mu\text{as}/\text{Hz}^{1/2}$ averaged for one second. The stability was modeled as a random-walk process with a buildup to a relative error of 10^{-7} in a time of 10^8 seconds.

Appendix H. Operational and Miscellaneous Considerations

Appendix H1. Entering the Counter-Rotating Orbits

In order to establish the counter-rotating orbits from a single launch of two satellites, one satellite is given a small positive coinclination and the other a negative one. Each then regresses through 90 deg due to the earth's oblateness, J_2 , until the counter-rotating orbits are attained. In order to complete the maneuver within one year, each coinclination must be set to about 3 degrees. At the end this must be removed giving a total inclination change of 6 degrees. To change the altitude of one satellite from 1500 km to 2500 km, a velocity increment of 413 m/sec is required which is equivalent to another 3.5 degrees of inclination change. Thus to accomplish the mission, a total inclination-change capability of 9.5 degrees must be carried. With monopropellant hydrazine, $I_{sp} = 220\text{ sec}$, this requires approximately 42 percent of the satellite's initial mass. The amount of Nitrogen gas required for drag-free operation is negligible by comparison, a few kilograms. During the year that the counter-rotating orbits are being established, the cavity can be baked using eddy currents from the spin-up motor to suppress outgassing, the drift of the two gyros can be cross checked, the severity of the rotor charging problem can be checked, the autocollimator and telescope readouts can be calibrated, and miniature low-accuracy geodetic drift experiments lasting about one month can be performed.

Appendix H2. Radiation Environment

The altitude range of 1000 to 2500 km enters the inner Van Allen belt, and starting at about 800 km there is a steep increase with altitude in the radiation dosage absorbed by a spacecraft [58]. The total unshielded dosage when one year is spent at each of the altitudes 1000, 1100, etc. to 2000 km is about 20×10^6 RAD; and for the range 1500 to 2500 km, it is about 40×10^6 RAD. In spite of these seemingly large values, a reasonable amount of shielding can reduce the total dose to acceptable levels in most cases. For example, using a 450-mil thick Aluminum shield, the calculated dose per year in a polar orbit at each of the altitudes 1500, 1600, etc. up to 2500 km. is 3.4, 4.3, 5.2, 6.2, 7.3, 8.2, 9.1, 10.0, 10.6, 11.2, and 11.6 kRAD for a total dose of 87.1 kRAD for an 11-year mission [59]. Electronic parts with a total dose resistance of 100 to 300 kRAD are available off the shelf, but typically not every satellite subsystem can be constructed with radhardened components. A typical non-radhardened linear IC has a hardness level between 30 and 100 kRAD; and in the worse case, this might limit the maximum altitude to 2200 km. This problem could be dealt with by beginning the mission between 1000 and 1300 km instead of 1500 km with some loss in cancellation from the orbital aberration, or the one-year data points could be reduced or overlapped. But the final decision will have to await a more detailed design study.

A shield thickness of 450 mils does not mean that the electronics must actually be enclosed in such a shield. Often the spacecraft structure, internal boxes, and skin can provide this amount of shielding. This is especially true for the experiment described here since the telescope and gyro assembly must be enclosed in a thermal-isolation shield, and the gyro must be surrounded by at least 0.4 cm of mumetal for the magnetic shield. Other than the linear circuits in the autocollimators, transcollimators, and telescopes; most of the other satellite subsystems can be constructed with radhardened parts. Because of the large number of photons per second, additional detector noise from the radiation is not a serious problem, and the A/D conversion takes place immediately after the first stages with the converters located at the detectors.

The solar arrays, however, cannot be shielded except by the 100-micron thick cover glasses (which stop the very damaging low energy protons); and at 1500 km they must absorb a total dose of about 8×10^6 RAD. In the case of Silicon cells, the total ten-year lifetime degradation due to 8×10^6 RAD is about 30 percent. With a total dose of 15×10^6 RAD, the degradation would be about 47 percent, but at about 50×10^6 RAD other effects come into play and the cells would be totally destroyed. On the other hand Gallium-

Arsenide cells have only about 10 percent of the degradation of Silicon; and in addition, they are better for protons which is the most damaging radiation component at these altitudes. Thus it can be seen that although a vehicle operating between 1000 and 2500 km must be specifically designed to withstand the radiation environment, this problem can be solved for the gyro experiment described in this paper.

Appendix H3. Active Damping

Unless there is a failure where the rotor orientation is lost, the active damper would not be needed at all since the rotor would be initially caged with the flats correctly aligned; and the torque motor would be used to maintain this alignment during uncaging and during the orbit change maneuvers when the rotor was not spinning. As a backup, however, an active damping system will be included. Coarse active damping is accomplished using the method of hemispheric torquing developed by Parkinson [33]. The signal pulse which marks the meridian passage of the north flat and hence the northern hemisphere can be obtained by a light pulse from the line of fiber-optic light sources and receptors shown in Figure 1 due to the optical flat. Alternatively if a satisfactory method of darkening the rotor can be found, the original Parkinson-VanPatten pattern can be used. In this case the transcollimators may have to be tilted slightly out of the plane of the equator. The transition from coarse active damping to acquisition of the optical flat by the autocollimator is done either open loop or with the Parkinson-VanPatten equatorial markings, and fine damping with the autocollimator is done using the algorithms developed by Parkinson and McKinley [33, 54]. If it can be realized, the Parkinson-VanPatten pattern is by far the better solution; and the array of fiber-optic sensors has only been considered because of the potential difficulties of darkening the rotor.

Appendix H4. Absolute Temperature Control

Absolute temperature control of the thermal enclosure will be done with heater strips attached to the outside. The heaters will be used to control the temperature to about 0.1 kelvin. Flight qualified heater strips have now been developed to a very advanced state, and the use of a great number of heaters to control absolute temperature is now standard practice on modern satellites. For this reason it has been decided to take advantage of this development to simplify the design and to create a more stable thermal environment for the telescope.

Appendix H5. Planetary Structure of the Reference Star

Planets with a star/planet mass ratio of 300,000 (earth sized) cause their central body to move in a circle with a radius of $3 \mu\text{as}$ -parsecs/AU with the period of the planet. For example, a star at a distance of 6 parsecs with the mass of the sun would oscillate one μas due to an earth-sized planet two AU from the star. When the two relativity measurements are added instead of subtracted, the reference star's proper motion in declination can be seen; and the experiment is sensitive enough to detect a motion of this amplitude. This possibility has not yet been studied in detail.

Appendix H6. Testing

All of the instruments and the gyro can be fully end-to-end tested before launch. For example in the case of the autocollimator, it can be tested either with the rotor spinning or nonspinning. A nonspinning rotor can be placed on an optical bench with two autocollimators front and back so that the rotor can be rotated slightly and the resulting angle change read out by the autocollimators. A spinning rotor in an electric bearing on a three-axis table can be tested by rotating the table and comparing the outputs of the two autocollimators against each other and the table rotation.

It is sometimes mistakenly said that an unsupported gyroscope cannot be tested prior to orbit. In fact every thing but the gyro drift (which can't be tested in any case no matter what gyro design is used but which was partly checked by the 1972 flight) can be tested by mounting the rotor in an electric bearing on a three-axis table. Since the purpose is to test the spin motor, the active damper, the flat alignment accuracy, and the rotor quality including roundness and CM offset; it is of no importance that the rotor is suspended since the only torque which could cause an error is the rotor-fixed component which can be accurately accounted for. The gyro drifts during testing are removed by tracking with the three-axis table so that no eddy-current torques need be applied during a test run. An ESG on the other hand must be spun up and tested prior to flight because the narrow $30\text{-}\mu$ gap and the possibility of low-temperature whiskers requires that it be demonstrated that the gap is entirely clear. The one-cm gap of the USG guarantees that the gyro will be completely free and fully functional in the drag-free mode if it functions correctly in an electric bearing.

Appendix H7. Four Gyros Versus One

The question of cross checking the gyro drift is important. In a given satellite only one gyro can be un-

supported, and the only way to have additional gyros for cross checking is to electrically support them. Additional ESGs, however, are expensive, unreliable, add complexity, and impose constraints on the USG which worsen its performance. For example, they restrict the spin speed of the satellite due to disturbing torques on the ESGs from centrifugal force; and a slower spin speed worsens the thermal isolation and the attitude control accuracy. In addition the satellite becomes much larger, and it is difficult to retain a form such that it is a major-axis spinner since the additional gyros must lie on the spin axis. It turns out that there are several better ways to cross check the gyro drift than multiple gyros in one satellite: 1) Probably the best cross check is to do repeated measurements versus altitude since the scatter in the data gives the overall system errors, not just the gyro drift. 2) By launching two or more satellites, the gyros can be compared with one another without the possibility of a common-mode error which could occur for gyros together in one satellite¹¹. 3) In an experiment which does the geodetic and frame dragging experiments separately, the cross axis can be used to check the drift of the experiment axis. 4) In the experiment with counter-rotating orbits, the two orbits also give a measurement of the frame-dragging drift which can be compared with the gyro result. 5) The AC-USG is a very simple device and its drift performance can be accurately calculated so that much greater confidence may be had in this gyro than in an ESG or an ESG with a gas spinup channel in the cavity. This is especially true in light of the 1972 drag-free flight since the gap and cavity design in that satellite were very similar to the AC-USG. A pure unsupported gyroscope is uncoupled from the rest of the universe to an extraordinary degree.

References

- [1] B. Lange, Phys. Rev. Lett. **74**, 1904-1907, (13 Mar 1995).
- [2] B. Lange, *The Unsupported Gyroscope With Autocollimator Readout, a High-Accuracy Design for the Relativity Gyro Experiment*, Unpublished.
- [27] Lange, B., *Techniques for a High-Precision Frame-Dragging Measurement Using an Unsupported Gyroscope in a Drag-Free Satellite*, Presented at the 8th Marcel Grossmann Meeting, Jerusalem, 22-28 June, 1997.
- [28] Gravity Probe B: I, II, and III, p. 1632, 382, 394. *Proc. 6th M. Grossmann Meeting*, World Scientific (1991). J. Turneure, Stanford Phys. Colloquium
- (Feb. 1994). Saps Buchman et al., *The Relativity Mission Gyroscopes*, pp. 1533-1535, Seventh Marcel Grossmann Meeting, *ibid*. See also the plenary talk by C. W. F. Everitt and the papers by S. Buchman, M. Meifetz et al., D. Bardas, and B. Muhlfelder et al. in the parallel session on GR in Space in the 8th Marcel Grossmann proceedings (in preparation).
- [32] B. Lange, Ph.D. Thesis, SUDAER¹² Report No. 194, June 1964. AIAA Journal, **2**, 9, 1950 (1964). *Unconventional Inertial Sensors Symposium Proc.*, Nov. 1964, Center for Aerosp. Inf., Baltimore, MD (66X-14701). *Third Interim Report: Advanced Research in Guidance, Control, and Instrumentation*, Jan. 1966, Stanford Engineering Libr. (SUAA-6604) or AFAL Wright-Patterson AFB (TECE-39860).
- [33] B. Parkinson and B. Lange, J. Spacecr. Rockets, **7**, 6, 667; **7**, 6, 675 (1970). B. Lange, J. Spacecr. Rockets, **9**, 2, 96 (1972).
- [36] R. V. Jones and J. C. Richards, J. of Sci. Instr., **36**, 2, 90 (1959). R. V. Jones, J. of Sci. Instr., **38**, 2, 37 (1961).
- [39] APL Technical Digest, **12**, No. 2, (1973). J. Spacecr. Rockets, **11**, 9, 637 (1974).
- [41] Standish, E. Myles, Ephemeris Specialist, NASA Jet Propulsion Laboratories, Personal communication.
- [42]. Davis, George W., Center for Space Research (CfSR), University of Texas at Austin, data on Topex and other satellite programs from Doris, SLR, and GPS tracking, Personal Communication.
- [43] Lange, B., *The GP-B Reference Star*, GP-B Technical Report S0194, June 4, 1993. *Noise Equivalent Angles and Detector Current Levels for the VLBI Radio Stars and Rigel By the Method of Spectral Integration*, GP-B Technical Report S0225, February 4, 1994.
- [47] Cannon, R. H. Jr., "Requirements and Design for a Special Gyro for Measuring General Relativity Effects from an Astronomical Satellite," *Kreiselprombleme*, edited by H. Ziegler, Springer-Verlag, Berlin, 1963, pp. 91-118.
- [48]. *The 1999 Astronomical Almanac*, U. S. Government Printing Office, p. K6.
- [49] K. R. Lorell, Ph.D. Thesis, SUDAAR¹² Report No. 422, Apr. 1971.
- [50] *U. S. Standard Atmosphere, 1976*, NOAA, NASA, USAF, Washington, DC, October, 1976.

¹² SUDAER, Stanford University Department of Aeronautical Engineering Report; and SUDAAR, Stanford University Department of Aeronautics and Astronautics Report: Ph.D. theses mostly in AA and EE available in the Stanford Engineering Library or directly from the Department of Aeronautics and Astronautics.

¹¹ Interestingly it has also turned out that two or more satellites are cheaper than solving the many problems associated with several gyroscopes in a single satellite.

- [51] Klinger, David L., *Error Modeling of Precision Orientation Sensors in a Fixed Base Simulation*, SUDAAR¹² Report No. 481, Ph.D. Thesis, July 1974.
- [52] Lange, B., *The Two-Color Transcollimator, a Precision Position Detector for a Satellite Two-Sphere Equivalence-Principle Experiment*, Presented at the 8th Marcel Grossmann Meeting, Jerusalem, 22-28 June, 1997.
- [53] R. V. Plank, *Optical Flat Placement on Almost Spherical Gyro Rotors*, Engineering Thesis, Stanford University Department of Aeronautics and Astronautics, Aug. 1965.
- [54] H. L. McKinley, Jr., *The Stability and Control of the Principal Axes of Inertia of Almost Spherical Bodies*, Ph.D. Thesis, SUDAAR¹² Report No. 325, Feb. 1968.
- [55] W. N. Blanchard, *The Readout-Axis Stability of Elastic, Nearly Spherical Gyro Rotors*, Ph.D. Thesis, SUDAAR¹² Report No. 431, Sept. 1971.
- [56] Deimel, Richard F., *Mechanics of the Gyroscope, the Dynamics of Rotation*, Dover Publications, 1950, frontispiece.
- [57] Meisinger, Reinhold, Personal communication. Gottman, M., *Mechanical Coupling between Thermal Deformation of Satellite Structure and an Inner Instrument Truss Isolated by a Single Joint*, Diplomarbeit, Labor für Fahrzeugsimulation and FEM, Ohm Fachhochschule, Nürnberg, 1996.
- [58] Wertz, James R. and Larson, Wiley J. (Editors), *Space Mission Analysis and Design*, Kluwer Academic Publishers, Boston, 1991, Chapter 8.
- [59] Wong, Frankie, Personal communication. Computer runs using the CRRES Radiation Model.

Detailed Acknowledgments

My former students, William N. Blanchard, Alan Fleming, Kenneth Lorell, Howard L. McKinley, Jr., Bradford Parkinson, Robert Victor Plank, and J. David Powell all worked on some part of the AC-USG design as part of their thesis research. Their work was principally directed toward the gyro readout system, although David Powell and Alan Fleming made

important contributions to the drag-free design itself. Furthermore, Alan Fleming accurately computed the sum of the gravitational attraction on the proof mass of all of the component parts of the spacecraft for the 1972 drag-free spacecraft thus making it possible to achieve the performance of 0.5×10^{-11} g. Richard VanPatten and Robert Clappier did all of the electronics for the student experiments and for the flight version of the drag-free control system. F. E. Futterer built the polishing apparatus and polished the first optical flats on the gyro rotors. In more recent times I have engaged in many stimulating discussions with Bradford Parkinson and Gaylord Green which greatly improved the design.

Professor Robert Cannon was my thesis advisor and supported the research on the Unsupported Gyroscope. Dan DeBra managed the program for the first drag-free satellite ever flown, developed the very-low-force continuous cold-gas thrusters, and argued convincingly for counter-rotating orbits instead of co-rotating orbits at different altitudes in spite of the large amount of propellant and the year needed to establish them. Andrew Buffington took a considerable amount of his personal time to examine the telescope design, identify critical areas, and suggest useful approaches. Francis Everitt conceived of calibration by orbital aberration, made significant contributions to the calculation of the gyro torques, the experimental goals, and the significance of the results to gravitational physics. Professor Leonard Schiff conceived of the original experiment at Stanford and was Ken Nordtvedt's thesis advisor. Reinhold Meisinger, an expert in finite-element methods (FEM), volunteered to have one of his students (M. Gottman) calculate the mechanical coupling between the spacecraft structure and the inner truss structure; and he invented a method to circumvent the limit of precision of classical FEM programs for the maximum dynamic range between input and output. Frankie Wong used his personal time to make special computer runs to calculate the radiation-dose levels which would be encountered in a polar orbit in the altitude range of 1500 to 2500 km.